PHILOSOPHICAL MAGAZINE A, 1996, VOL. 73, NO. 6, 1529–1563

Quasicontinuum analysis of defects in solids

By E. B. TADMOR, M. ORTIZ and R. PHILLIPS

Division of Engineering, Brown University, Providence, Rhode Island 02912, USA

[*Received 10 July 1995 and accepted in revised form 14 October 1995*]

ABSTRACT

We develop a method which permits the analysis of problems requiring the simultaneous resolution of continuum and atomistic length scales—and associated deformation processes—in a unified manner. A finite element methodology furnishes a continuum statement of the problem of interest and provides the requisite multiple-scale analysis capability by adaptively refining the mesh near lattice defects and other highly energetic regions. The method differs from conventional finite element analyses in that interatomic interactions are incorporated into the model through a crystal calculation based on the local state of deformation. This procedure endows the model with crucial properties, such as slip invariance, which enable the emergence of dislocations and other lattice defects. We assess the accuracy of the theory in the atomistic limit by way of three examples: a stacking fault on the (111) plane, and edge dislocations residing on (111) and (100) planes of an aluminium single crystal. The method correctly predicts the splitting of the (111) edge dislocation into Shockley partials. The computed separation of these partials is consistent with results obtained by direct atomistic simulations. The method predicts no splitting of the Al Lomer dislocation, in keeping with observation and the results of direct atomistic simulation. In both cases, the core structures are found to be in good agreement with direct lattice statics calculations, which attests to the accuracy of the method at the atomistic scale.

§ 1. INTRODUCTION

The analysis of the structure of crystal defects such as dislocations and grain boundaries requires consideration of anharmonic effects on the scale of the lattice. Lattice statics and molecular dynamics based on interatomic interactions provide a powerful and accurate tool of analysis on this scale. Recent examples of application of these techniques may be found in the work of Gallego and Ortiz (1993), Mills, Daw and Foiles (1994), Sutton and Pethica (1990) and Arias and Joannopoulos (1994). Atomistic analyses have provided useful insights into phenomena controlled by discrete lattice effects (see, e.g., Christian (1983) for a review). At the other end of the spectrum, the macroscopic deformation behaviour of crystals may involve dislocation densities as high as $10^{13}\ \mathrm{m}^{-2}$. An area of $1\ \mathrm{mm}^2$, e.g., near the tip of a crack, may be crossed by as many as 10^9 dislocations. This precludes consideration of individual dislocations at the macroscopic scale, and has spurred the development of constitutive models which treat dislocations and other defects as continuously distributed objects (see, e.g., Cuitiño and Ortiz (1992) for a review).

An intermediate scale, of the order of a few hundred nanometres, is presently emerging as the focus of increasing attention in applications such as nanoindentation (Pharr, Oliver and Clarke 1990, Harvey, Huang, Venkataraman and Gerberich 1993)

and the investigation of the brittle/ductile transition in high purity materials (Chiao and Clarke 1989, Brede 1993). This scale is presently beyond the reach of conventional atomistic and continuum methods alike. Thus, the number of atoms involved in these simulations is often in excess of 10^8, which rules out purely atomistic models. However, the deformation processes of interest involve discrete dislocations in number which are too small to be described adequately by macroscopic crystal plasticity models. This is the scale preferentially addressed in the present work.

We aim for one theory with the following attributes. At the macroscale, the theory should reduce to continuum crystal elasticity, with its usual properties of material frame indifference and crystal symmetry (Gurtin 1981, Milstein 1982). At the microscale, the theory should be built upon reliable interatomic interactions, incorporate a lattice parameter and possess all the lattice invariance properties expected of a crystal lattice. We note that the incorporation of the lattice parameter as an intrinsic length necessarily renders the theory non-local. Of particular concern is that the theory enables an accurate treatment of lattice defects such as dislocations, should these defects arise. At intermediate length scales, or mesoscales, the theory should exhibit a continuous or seamless transition from the lattice to the continuum realms. In particular, we rule out the patching of lattice and continuum models, as has been common practice in the past (Kohlhoff, Gumbsch and Fischmeister 1991).

This paper is devoted to the development of a quasicontinuum theory of the type just described. Viewed from a continuum perspective, the theory is predicated on the use of atomistic potentials to describe the constitutive response of the crystal. The atoms are constrained to move in accordance with the continuum displacement field, which enables the computation of energies and forces from local lattice calculations. By this construction, the resulting continuum automatically satisfies material frame indifference and exhibits all the symmetries of the crystal. It also possesses lattice invariance, i.e., its energy is invariant with respect to distortions of the reference configuration which bring the lattice into coincidence with itself. In particular, the energy density is periodic under crystallographic slip. A far-reaching consequence of this periodicity is the lack of quasiconvexity of the energy functional (Chipot and Kinderlehrer 1988, Fonseca 1988), which opens the way for lattice defects such as dislocations to develop stably. The relaxation of functionals lacking quasiconvexity requires consideration of minimizing sequences of deformations which exhibit structure on increasingly finer scales (Ball and James 1987, Dacorogna 1989). From a computational standpoint, this necessitates multiple-scale analysis capability enabling the simultaneous resolution of macroscopic and microscopic features in the solution.

In our approach, the scales of interest are resolved by recourse to adapative meshing: we refine the mesh near regions of highly non-uniform deformation such as dislocation cores and crystal boundaries, while discretizing regions of slowly varying deformation coarsely. In this manner, a significant reduction in the number of degrees of freedom is achieved relative to purely atomistic methods, without relinquishing full atomistic resolution where needed. To prevent the displacement field from developing unphysical sublattice-scale structure, the lattice parameter is taken to set a lower bound for the mesh size. This physical bound is enforced by checking the process of mesh refinement when elements attain dimensions commensurate with the lattice parameter. The crystal thereby takes on a character similar to Kunin's quasicontinua (Kunin 1982), and we name the theory accordingly. However, it should be noted that Kunin's quasicontinuum is obtained by restricting

the Fourier transform of the displacement field to the first Brillouin zone of the crystal. This is in contrast to our theory, which employs a cut-off length in real space.

The elements in the model behave locally or non-locally depending on their size, extent of deformation and energy: small, highly deformed and highly energetic elements are treated non-locally, while all other elements are treated locally. A local element 'sees' the state of deformation within its domain only, while non-local elements see the deformation of neighbouring elements as well. The non-local treatment of elements lying in the vicinity of slip planes and crystal boundaries is required for the model to properly account for surface and stacking-fault energies. In the coarse mesh-size limit, the crystal becomes indistinguishable from a nonlinear elastic crystal obeying the Cauchy–Born rule (Milstein 1982). In the fine-mesh limit, the theory reverts to lattice statics. Consequently, from an atomistic perspective our quasicontinua may simply be regarded as atomistic lattices subjected to kinematic constraints, namely, those introduced by the finite element interpolation. These constraints have the desirable effect of eliminating excess atomistic degrees of freedom in regions where the deformation field varies slowly on the scale of the lattice.

The structure of the paper is as follows. The quasicontinuum formulation of the general boundary value problem is developed in § 2. There the conventional finite element formulation is contrasted with the present approach with particular emphasis on the way in which constitutive phenomenology results from atomistic calculations. A range of issues such as the non-local aspects of the theory and algorithms for solving the resulting boundary value problems are also discussed. The analyses of three types of dislocations in aluminium collected in § 3 serve as stringent tests of the ability of the theory to account for lattice defects accurately. Closing remarks on the relative merits and future prospects of the theory are given in § 4.

§ 2. The quasicontinuum formulation

2.1. *Overview*

In continuum mechanics, solids are modelled as continuous media with appropriate average material properties. Each local neighbourhood of the solid may be regarded as a continuum particle (Weiner 1983), representative of a large region on the microscale. At this level of description, the energy of the solid is an extensive property, and follows locally from the deformation of each continuum particle. This requires the size of the continuum particles to be small relative to the distance over which the continuum fields are allowed to vary appreciably. The constitutive theory appropriate to each case also varies in accordance with the coarseness of the description. By contradistinction, atomistic theories regard solids as collections of atoms whose interaction is modelled by an appropriate energy function. By recourse to this atomistic 'microscope', it is possible to obtain a great deal of detail at the scale of the crystal lattice. However, present computer hardware places stringent limits on the number of atoms which can be included in atomistic models especially if, as envisioned here, the crystal lattice contains defects. Perhaps a more fundamental objection to large-scale atomistic simulations is that, frequently, the vast preponderance of the lattice deforms smoothly and closely obeys continuum elasticity. Under such conditions, it may be unnecessary and unduly wasteful to account for every atom in the lattice.

The quasicontinuum (QC) theory developed here marries these two contrasting views, thus enabling a seamless description of solids exhibiting structure on atomistic

and continuum scales. The continuum framework and continuum particle concept are retained, but the macroscopic constitutive law is replaced by one based upon direct atomistic calculations (see fig. 1). The continuum particle is identified with a small crystallite of radius R_c surrounding a representative atom. This crystallite, which constitutes a true collection of atoms, is distorted according to the local continuum displacement field. The energy of the crystallite is computed from an appropriate atomistic model. Since the energy of each point is obtained directly from atomistics, key properties of the crystal, such as crystal symmetries and slip invariance, are automatically introduced into the description. The continuum displacement fields are parametrized by the finite element method (FEM). As is standard in the FEM, the solid is partitioned into a finite number of regions, or 'elements'. The deformation within each element is interpolated from the corresponding nodal displacements, which thus become the sole unknowns of the problem. In the quasistatic case, the energy is computed as the sum of the energies of the representative crystallites and the finite element solution follows by energy minimization.

In order to compute energies, the deformation of the crystallite and the continuum displacement field need to be placed in correspondence. A standard approach often followed in molecular theories of crystal elasticity is the Cauchy–Born rule (Milstein 1982, Ericksen 1984) where the atomic positions are related to the continuum fields through the local deformation gradient $\mathbf{F}$. The deformed crystal structure is obtained by applying $\mathbf{F}$ to the undeformed crystal lattice basis and then reconstructing the crystal from the altered base vectors (see fig. 2). In this manner each continuum particle is represented by an infinite crystal undergoing homogeneous deformation. In the context of our quasicontinuum theory, we shall refer to this limit as the local QC formulation.

Although it is elegant and straightforward to implement, the local formulation suffers from several drawbacks that make it necessary to expand the formulation to deal with non-local effects. The primary difficulty is that due to the homogeneous nature of the deformation in the local formulation, it becomes impossible to model important inhomogeneous structural features such as stacking faults.

Real stacking faults correspond to two undistorted crystalline half spaces slipping over each other by a non-lattice translation vector, and are therefore non-uniform. Within the local QC framework such structures can only be modelled via a simple shear deformation, which except for the two atomic layers directly adjacent to the slip plane, results in a completely different structure than is found in a real stacking fault. The stacking fault energy plays a crucial role in many crystalline processes and when computed in the local formulation leads to a spurious result. This is demonstrated in fig. 3, where a fcc stacking fault is presented. In (*a*), the correct stacking fault structure is represented, where we see the top half-plane has slipped over the bottom plane in the $[1\bar{2}1]$ direction, creating an intrinsic stacking fault $ABCA|CABC$. Frame (*b*) shows the simple shear version of (*a*) and it is seen that the crystal has been transformed to its twin variant (i.e. $ABCABC\ldots$ stacking is transformed to $CBACBA\ldots$) which is energetically degenerate with the original structure. Thus, for a fcc crystal the local QC formulation predicts zero stacking fault energy.

Other difficulties associated with purely local formulations are that crystals modelled in this fashion do not have a well-defined Peierls stress and do not allow for interface defects such as free surfaces, grain boundaries or other heterogeneous

Fig. 1

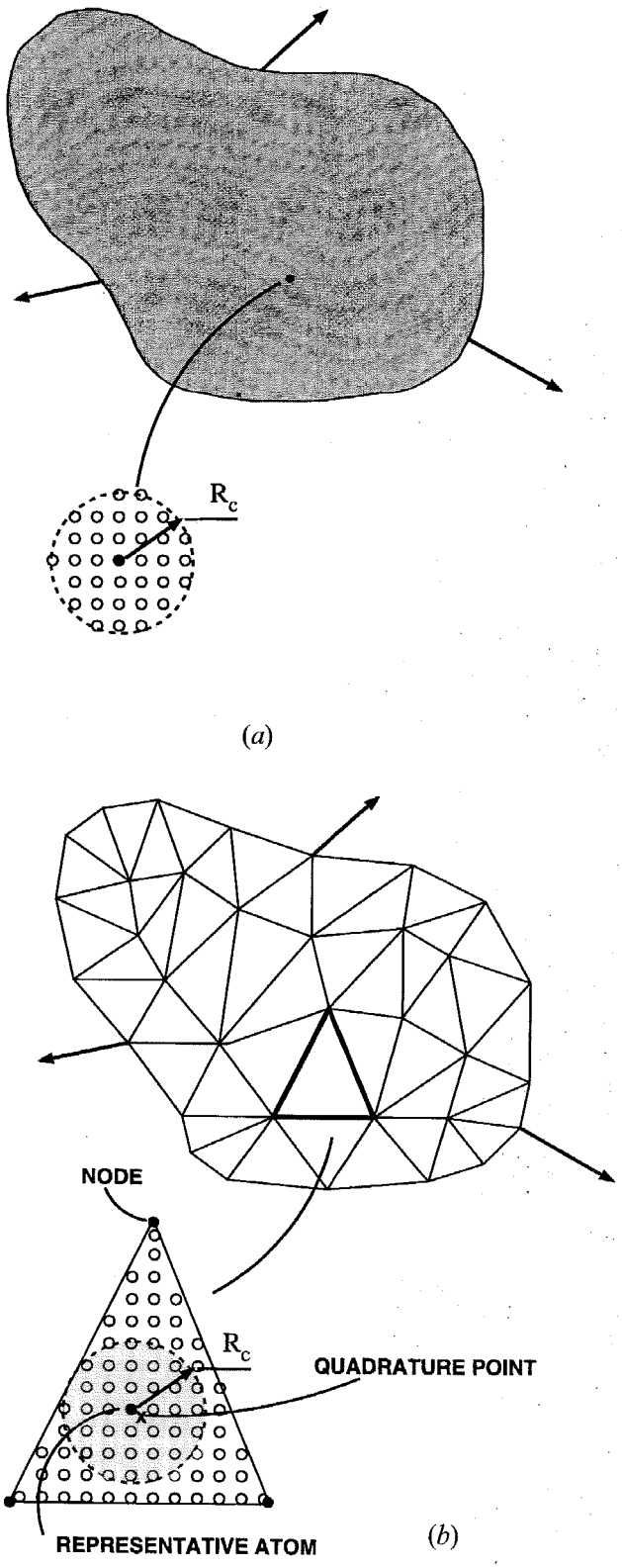

Schematic of the quasicontinuum concept. (*a*) Every point in the continuum is modelled by a representative atom (black) embedded in a crystallite of radius R_c. (*b*) FEM discretization of the solid in (*a*), showing element, underlying crystal lattice and representative atom.

Fig. 2

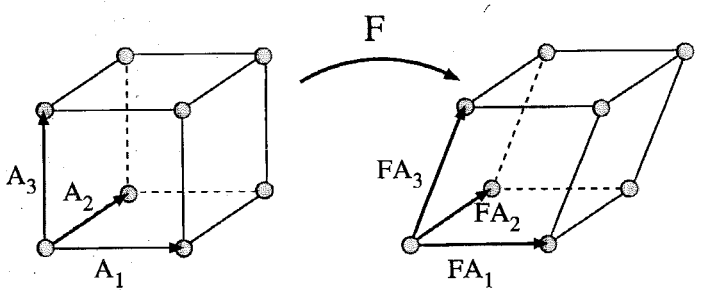

The Cauchy–Born rule: an undistorted lattice with lattice vectors $\mathbf{A}_I$ is mapped to the deformed configuration by application of the local deformation gradient $\mathbf{F}$.

Fig. 3

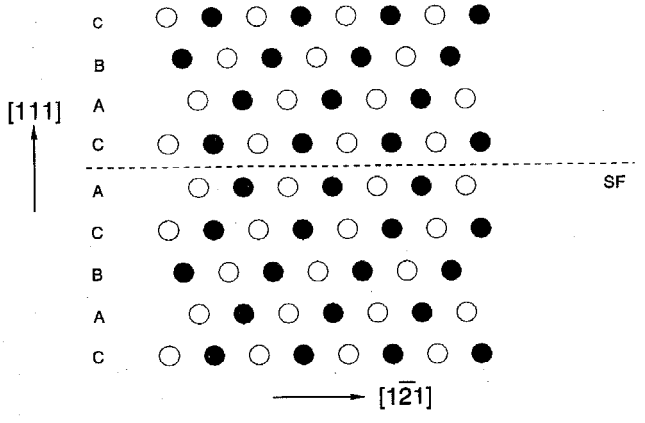

(*a*)

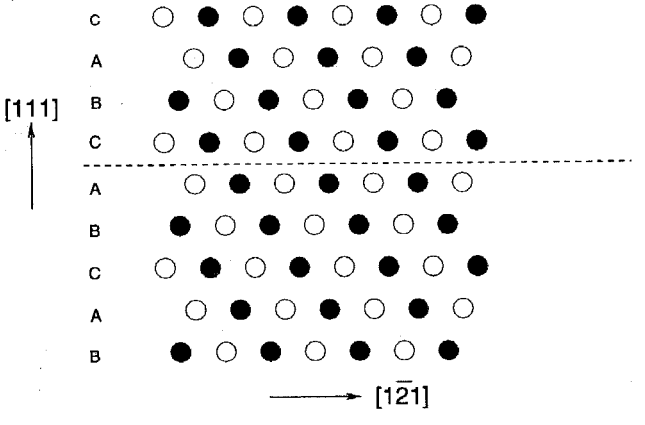

(*b*)

Stacking fault in a fcc crystal (atom shading indicates different out-of-plane postions). (*a*) Actual fcc stacking fault structure, (*b*) atomic positions implied by a simple shear model of the SF.

interfaces. Furthermore, the lattice parameter which serves as the crystal's intrinsic length scale is lost in the Cauchy–Born process allowing the energy minimization routines to develop structure on sublattice length scales, a clearly unphysical situation. These deficiencies become critical near defect cores, further emphasizing the need to expand the formulation to deal with non-local effects.

In the non-local QC formulation each atom within the representative crystallite is displaced according to the actual continuum displacement field at its position. This implies that the position of the atom $\mathbf{R}_n$ after deformation is given by $\mathbf{r}_n = \mathbf{R}_n + \mathbf{u}(\mathbf{R}_n)$, where $\mathbf{u}$ is the continuum displacement field. The local and non-local formulations are equivalent as long as the element is sufficiently large as to entirely contain the representative crystallite centred about its quadrature point (see fig. 4); however, as the elements become smaller than R_c, members of the representative crystallite will fall inside different elements and experience a non-uniform displacement field (see fig. 5). In this manner the modelling of stacking faults becomes straightforward. The use of non-local elements near the stacking fault plane captures the true non-uniform deformation and as a consequence returns the correct associated energy.

The non-local formulation also extends the method so that problems such as those involving free surfaces, grain boundaries and other interfaces can be treated as well. Elements smaller than the representative crystallite radius R_c placed near such an interface will, because of non-locality, have representative atoms that experience either undercoordination, such as at a free surface, or will include atoms of different species such as at a bi-material interface, or include atoms arranged in a different crystal orientation for a grain boundary (see fig. 6). If we choose not to include the interfacial effects we simply constrain the size of the elements near the interface to be larger than R_c. This feature becomes very useful when, for example, we wish to model an effect far from the crystal surface (such as a dislocation in an infinite crystal) and do not wish the solution to be contaminated by surface effects.

In general, then, the mesh is primarily composed of local elements away from defects and other severe non-uniformities with non-local elements introduced as

Fig. 4

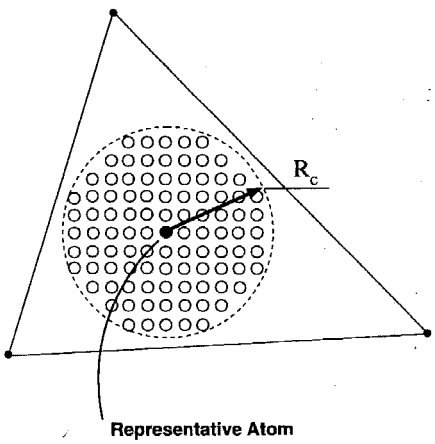

Local QC/FEM element (small black circles at triangle corners represent nodes, larger circles within the dashed perimeter are atoms belonging to the representative crystallite).

Fig. 5

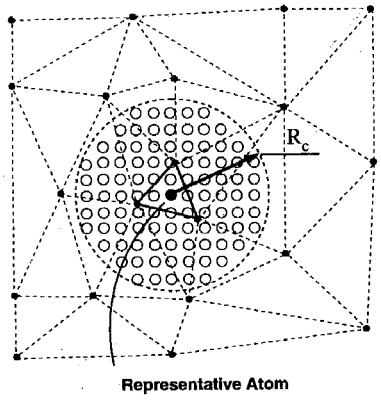

Non-local QC/FEM element (solid triangle) surrounded by nearby elements (dashed triangles)—symbols have same meaning as in previous figure.

Fig. 6

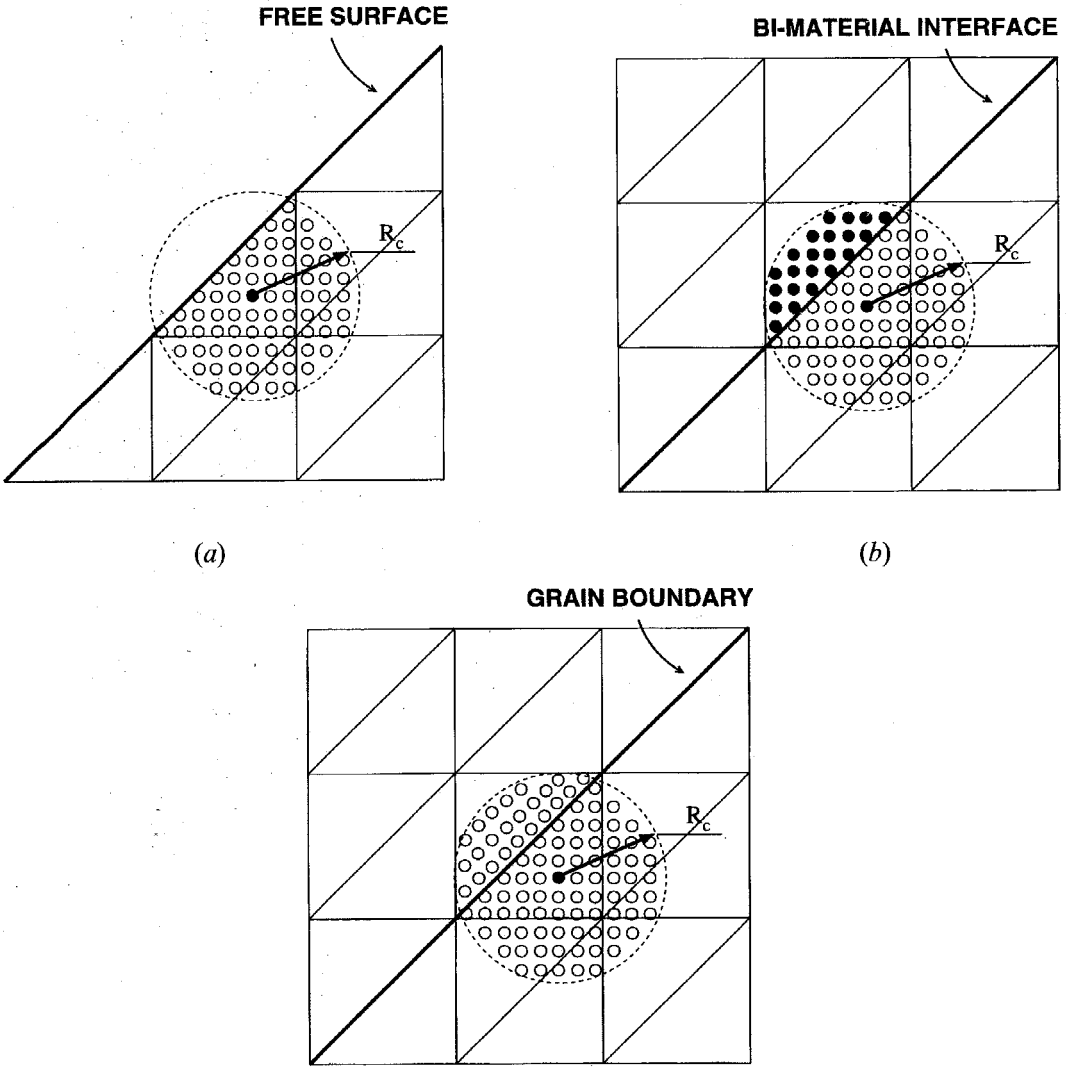

Interfacial effects captured by a non-local element placed near (*a*) a free surface, (*b*) a bi-material interface and (*c*) a grain boundary.

necessary to capture these effects. A criterion for automatic selection of the local against non-local status of each element is presented in § 2.6.

One result of the introduction of non-local elements into a local QC/FEM mesh is the loss of centrosymmetry at non-local element nodes. Except for the special case of a uniform mesh, non-local nodes within the mesh are not surrounded by a symmetric distribution of representative atoms. As a result, the out-of-balance force residual is non-zero for the undistorted mesh, implying an equilibrium energy lower than the perfect crystal cohesive energy. Similar effects have been observed by Bassani, Vitek and Albert (1992) in their investigation of atomic-level elastic properties of interfaces. Relaxation of the spurious non-zero forces reveals the overall effect to be negligible. For example, in models of dislocations in Al, the maximum atomic displacements observed after relaxation of these forces were less than 0·1 Å and the reduction in energy was of the order of 10^{-5} eV atom^{-1} (this should be contrasted with typical atomic relaxation energies of 0·1 eV atom^{-1}). A further example of non-centrosymmetric effects is given in § 3.2 where the QC solution for a Lomer dislocation is presented.

2.2. *Constitutive models*

The formulation of reliable constitutive relations is an area of interest to mechanics and materials science alike. The traditional finite element approach has been to postulate a constitutive relation thought to be appropriate for the problem of interest. Our approach differs in that it appeals to the microscopic underpinnings to yield a model for the mechanical response of a material. The use of atomistically derived constitutive relations has the immediate effect of lending our model all relevant crystal symmetries. Thus no presuppositions on crystal behaviour have to be made at the constitutive level and the crystal is free to assume any configuration dictated by equilibrium. Most important of the symmetry properties implied by adopting this approach is slip-invariance, which refers to the fact that the energy of the solid is invariant under crystallographic slip. Slip invariance in the continuum is described by the one-parameter family of deformation mappings

$$\mathbf{H}(\gamma) = \mathbf{I} + \gamma \mathbf{s} \otimes \mathbf{n}, \tag{1}$$

where $\mathbf{n}$ is the normal to the slip plane, $\mathbf{s}$ is a vector in the slip direction, γ is the slip strain and $\mathbf{I}$ is the identity matrix. By lattice invariance, the energy density $W(\gamma)$ is periodic in γ with period b/d, where $b = |\mathbf{b}|$ is the magnitude of the translation vector and d is the distance between adjacent crystallographic planes perpendicular to $\mathbf{n}$. This effect can be seen in fig. 7 where the dependence of energy density on the slip and the associated crystal structures are presented. In the figure, A corresponds to a perfect undistorted crystal, B corresponds to a metastable state where the force is zero but the energy is maximal and in C the perfect crystal structure is restored. In the wake of a dislocation we expect the atoms on the slip plane to occupy energy wells that correspond to position C, indicating the vital role of slip invariance in allowing for the presence of dislocations and other stable defects in the crystal.

Our basic approach is independent of the choice of any particular atomistic scheme for computing the energy at the atomistic scale. The basis of our calculations is illustrated schematically in fig. 1(*b*). A global origin in the undeformed configuration relating the continuum finite element model to the underlying crystal structure is set. Then for every quadrature point in the FEM mesh (where the continuum fields are sampled for numerical integration) the nearest atom is selected as a representa-

Fig. 7

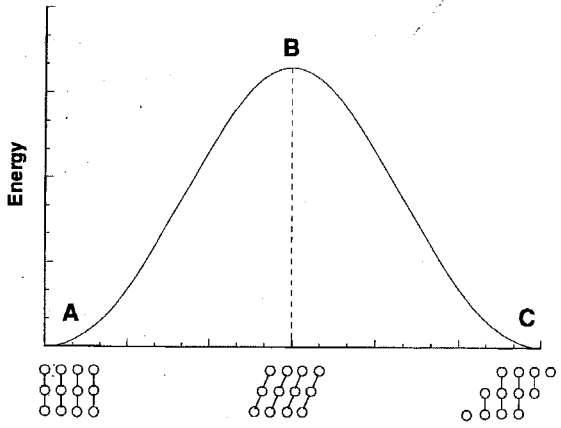

Invariance of strain energy under shear as obtained from microscopically derived constitutive model.

tive atom. We then deform a small neighbourhood around that atom either according to the local deformation gradient tensor **F** if the element is deemed local (see § 2.4) or based on the actual displacement of every atom according to the global continuum displacement fields if the non-local formulation is used (see § 2.5). We can then compute the total energy of the representative atom using an appropriate atomistic model, and return to the FEM model the energy and its derivatives at the quadrature point. By refining the mesh and using the non-local model in highly strained regions, non-linear core effects will be picked up, while in less strained regions far from the core the local approximation will yield linear elastic behaviour.

Recent advances in the microscopic modelling of materials have resulted in a range of methods for computing the total energy of an assembly of atoms; methods ranging from pair potentials to the most sophisticated quantum mechanical calculations using density functional theory. In the end, each method involves compromises. Simple methods such as pair potentials, while fast and hence applicable to large systems, lack the accuracy and transferability to make them a viable candidate for quantitative analysis. On the other hand, density functional techniques, while highly accurate, are limited to the treatment of at most hundreds of atoms, leaving analysis of extended defects in complex environments still out of reach. In principle, any of these methods is applicable to our implementation of the quasicontinuum method.

For the purposes of illustration, we have implemented the embedded-atom method (EAM) (Daw and Baskes 1983) to yield total energies for the system of interest. In the EAM, the total energy of a crystal is given in terms of an embedding energy accounting for the interaction between the nuclei and surrounding electron gas, and a second term accounting for the self-interaction of the nuclei. In this context the strain energy density W is given by

$$W = \frac{1}{V} \sum_i [U_i(\rho_i) + \Phi_i], \tag{2}$$

where i runs over all atoms in the crystal, V is the total volume of the crystal, ρ_i is the ambient electron density at atom i, U_i is the energy required to embed atom i into

electron density ρ_i, and Φ_i is the total interaction energy of atom i with all neighbouring nuclei. This last term, which accounts for the short-range core–core repulsion is modelled as a pairwise interaction over all nuclei

$$\Phi_i = \frac{1}{2}\sum_{j(\neq i)} \phi_{ij}(r_{ij}), \tag{3}$$

where i and j run over all atoms in the crystal, ϕ_{ij} is a pairwise interaction potential between atoms i and j, and r_{ij} is the distance between atoms i and j

$$r_{ij} = |\mathbf{r}_i - \mathbf{r}_j|, \tag{4}$$

where $\mathbf{r}_i$ and $\mathbf{r}_j$ are the position vectors of atoms i and j, respectively. The electron density at atom i is approximated as the superposition of the electron densities due to the surrounding atoms at the location of atom i

$$\rho_i = \sum_{j(\neq i)} f_j(r_{ij}), \tag{5}$$

where f_j is the electron density generated by atom j at a distance r_{ij} from its core.

We have examined a range of different embedded-atom functions, but for the purposes of this paper have settled on the recently developed functions of Ercolessi and Adams (1993). A notorious flaw of embedded-atom type models has been their severe underestimate of stacking fault energies—a shortcoming that hampers their capacity to model dislocations. Through fitting *ab-initio* calculations for a range of material properties, the Ercolessi–Adams potentials have a substantially larger intrinsic stacking fault energy than competing EAM potentials for Al. As a result, significant improvements have been found in the dislocation core structures predicted by this method (Mills *et al.* 1994). It should be emphasized, however, that while we have chosen the embedded-atom method for the purposes of the present calculations, our use of atomistics to determine constitutive relations is not tied to any particular choice of atomistic calculations.

2.3. *Field equations and spatial discretization*

Consider a crystal occupying a reference configuration B_0 in R^3, which is referred to a material Cartesian frame $\{X_I, I = 1, 2, 3\}$. The crystal undergoes a motion described by a deformation mapping $\boldsymbol{\phi}(\mathbf{X}, t)$. The image of B_0 by $\boldsymbol{\phi}(\cdot, t)$ defines the deformed configuration B_t of the crystal at time t, which is referred to a spatial Cartesian frame $\{x_i, i = 1, 2, 3\}$. The deformation at time t of an infinitesimal material neighbourhood $\mathrm{d}V_0$ about a point $\mathbf{X}$ of B_0 is completely defined by the linear part of $\boldsymbol{\phi}(\cdot, t)$ at $\mathbf{X}$. This defines an affine mapping

$$\mathrm{d}x_i = F_{iJ}(\mathbf{X}, t)\,\mathrm{d}X_J, \tag{6}$$

where F_{iJ} are the components of the deformation gradient

$$F_{iJ}(\mathbf{X}, t) = \phi_{i,J}(\mathbf{X}, t), \tag{7}$$

where upper-case indices refer to the material frame, lower-case indices to the spatial frame, and $(\cdot)_{,J}$ indicates differentiation with respect to X_J. In invariant notation, $\mathbf{F} = \nabla_0 \boldsymbol{\phi}$, where ∇_0 denotes the material gradient operator.

We can now formulate the general boundary value problem. To this end, we partition the reference boundary ∂B_0 into a Dirichlet, or displacement, component ∂B_{01}, and a Neumann, or traction, component ∂B_{02}. The solid is subjected to pre-

scribed displacements $\bar{\boldsymbol{\phi}}$ on ∂B_{01}, and to prescribed tractions $\bar{\mathbf{T}}$ on ∂B_{02}. In addition, the solid is acted upon by body forces per unit volume $\rho_0\mathbf{B}$, where ρ_0 is the reference mass density and $\mathbf{B}$ is the body force field per unit mass. Stable configurations of the crystal are identified with the minimizers of the potential energy

$$\Pi[\boldsymbol{\phi}] = \inf_{\boldsymbol{\psi}}\left(\int_{B_0} W(\boldsymbol{\psi})\mathrm{d}V_0 - \int_{B_0}\rho_0\mathbf{B}\cdot\boldsymbol{\psi}\mathrm{d}V_0 - \int_{\partial B_{02}}\bar{\mathbf{T}}\cdot\boldsymbol{\psi}\mathrm{d}S_0\right), \tag{8}$$

where $W(\boldsymbol{\psi})$ is the strain energy density computed from some appropriate atomistic energy function, and the trial deformation mappings $\boldsymbol{\psi}$ belong to some suitable space of functions over B_0 satisfying the essential boundary condition $\boldsymbol{\psi} = \bar{\boldsymbol{\phi}}$ on ∂B_{01}.

Evidently, for small deformations of the crystal, the formulation reduces to conventional anisotropic elasticity. In this limit, energy minimizers are uniquely defined up to a rigid body motion. These conditions are commonly realized in regions of the crystal which are far removed from lattice defects. However, the fact that the strain energy density W is computed directly from an atomistic potential implies that it lacks quasiconvexity (Chipot and Kinderlehrer 1988, Fonseca 1988), which in turn makes it possible for energy minimizers to develop microstructure on a fine scale, including lattice defects such as dislocations. On this scale, the periodicity of the lattice, and the resulting periodicity of the energy function with respect to crystallographic slip, become all-important.

For reasons that will become apparent subsequently, an essential building block of the present approach is the introduction of a method of spatial discretization well suited to multiple-scale analysis. In solid mechanics applications, adaptive finite element methods have proved particularly powerful in this respect. We begin by partitioning the reference configuration B_0 into finite elements $\{\Omega_h^e, e = 1, \ldots, M\}$, where M is the number of elements, and h denotes a measure of the size of the mesh, such as the size of the smallest element. The deformation mapping and deformation gradients are discretized in the usual manner (Hughes 1987), namely

$$\boldsymbol{\phi}_h(\mathbf{X}, t) = \sum_{a=1}^{N}\boldsymbol{\phi}_a(t)N_a(\mathbf{X}), \tag{9}$$

$$\mathbf{F}_h(\mathbf{X}, t) = \sum_{a=1}^{N}\boldsymbol{\phi}_a(t)\nabla_0 N_a(\mathbf{X}), \tag{10}$$

where $a = 1, \ldots, N$ are the nodes in the mesh, N is the number of nodes, $\boldsymbol{\phi}_a(t)$ are the nodal coordinates at time t, and $N_a(\mathbf{X})$ are the interpolation, or 'shape', functions. The primary unknowns of the problem are now the nodal coordinates $\boldsymbol{\phi}_a(t)$. These follow from the constrained minimization problem

$$\Pi_h[\boldsymbol{\phi}_h(t)] = \inf_{\boldsymbol{\psi}_h}\left(\int_{B_0} W(\boldsymbol{\psi}_h)\,\mathrm{d}V_0 - \int_{B_0}\rho_0\mathbf{B}(t)\cdot\boldsymbol{\psi}_h\,\mathrm{d}V_0 - \int_{\partial B_{02}}\bar{\mathbf{T}}(t)\cdot\boldsymbol{\psi}_h\,\mathrm{d}S_0\right), \tag{11}$$

where the trial functions are of the form

$$\boldsymbol{\psi}_h(\mathbf{X}) = \sum_{a=1}^{N}\boldsymbol{\psi}_a N_a(\mathbf{X}), \tag{12}$$

and are required to satisfy the essential boundary conditions identically on ∂B_{01}. All integrals in eqn. (11) can be conveniently performed by numerical quadrature at the element level. For instance, the strain energy is computed as

$$\int_{B_0} W(\psi_h)\,\mathrm{d}V_0 \approx \sum_{e=1}^{M}\sum_{q=1}^{Q} w_q^e W(\psi_h(\xi_q^e)), \tag{13}$$

to within the accuracy of the numerical quadrature rule. Here, Q is the order of the quadrature rule, and w_q^e and ξ_q^e are the quadrature weights and points for element e. The use of numerical integration reduces all stress–strain calculations to the quadrature points of the elements. In our simulations, we use linear three-noded triangular elements with a one-point quadrature rule (Hughes 1987) and construct all meshes by automatic triangulation based on the Delaunay algorithm (Sloan 1987). The use of linear elements guarantees a smooth transition from non-local to local elements since the non-local formulation reduces to the local one for large elements in this case.

To solve the constrained minimization problem in (11) we can use either a Newton–Raphson (NR) solver with its powerful quadratic convergence properties, or a conjugate gradient (CG) approach followed by a NR polish when the initial guess is too far from the solution for NR to initially converge. In both cases we will require the first and second variation of the total potential energy Π_h with respect to the nodal degrees of freedom ψ_h, referred to in FEM terms as the global out-of-balance force residual and the global stiffness matrix, respectively. These are computed differently depending on whether the element is local or non-local and are given in §§ 2.4 and 2.5.

2.4. *Local quasicontinuum*

It remains to be shown explicitly how the energy and its variations are computed at a quadrature point given the continuum deformation fields there. In the local quasicontinuum formulation, it is imagined that each point in the solid is represented locally by an infinite crystal subjected to homogeneous deformation. A consequence of the homogeneity is the loss of the global origin linking the underlying crystal lattice to the continuum. As a result the choice of representative atom is immaterial since all atoms are equivalent. We can thus imagine our infinite crystal as surrounding a representative atom located at the origin. Following the Cauchy–Born approximation (Ericksen 1984), this infinite crystal is deformed according to the local continuum deformation gradient (see fig. 2). Consequently, if $\{\mathbf{A}_\mathrm{I}, \mathrm{I} = 1,2,3\}$ is a crystal basis, then the coordinates of its atoms are

$$\mathbf{X}(\mathrm{m}) = m_I \mathbf{A}_I, \quad \mathbf{m} \in Z^3, \tag{14}$$

where Z is the set of integers. The positions of the atoms in the deformed configuration are then taken to be

$$\mathbf{x}(\mathbf{m}) = \mathbf{F}\mathbf{X}(\mathbf{m}), \quad \mathbf{m} \in Z^3, \tag{15}$$

where $\mathbf{F}$ is the local deformation gradient which is constant within the element. In practice a region of radius R_c (taken to be about twice the potential cutoff radius r_c) is stored to represent the infinite crystal (see fig. 4). We must then ensure that the applied trial deformation $\mathbf{F}$ is not so severe as to bring atoms from outside the region R_c to within the cutoff radius r_c of the representative atom.

To account for this we introduce the concept of an *influence radius* associated with deformation **F**. This radius corresponds to the most distant point in the undeformed configuration that is mapped into the representative atom's cut-off sphere in the deformed configuration. This restriction can be neatly expressed as an eigenvalue problem, which leads to the following result:

$$R_{\text{inf}} = r_{\text{c}}\sqrt{\lambda_{\max}}, \tag{16}$$

where R_{inf} is the influence radius and $\lambda_{\max}$ is the maximum eigenvalue of $\mathbf{F}^{-\text{T}}\mathbf{F}^{-1}$. We thus require every trial deformation during the minimization process to satisfy $R_{\text{inf}} \leq R_{\text{c}}$, otherwise the deformation is rejected as overly severe. Failure to account for this effect can result in erratic behaviour during the bracketing and line search phases of the CG minimization (Press *et al.* 1992).

Once the trial deformation has been accepted, the strain energy density W follows as a function of **F** and can be computed using the underlying atomistic method. The local contributions to the out-of-balance force residual and global stiffness matrix follow as

$$\frac{\partial \Pi_h}{\partial \boldsymbol{\psi}_a} = \sum_e^{\text{local}} \int_{\Omega_h^e} (\mathbf{P}\cdot\nabla_0 N_a)\,\mathrm{d}V_0 - \int_{B_0} \rho_0 \mathbf{B} N_a\,\mathrm{d}V_0 - \int_{\partial B_{02}} \bar{\mathbf{T}} N_a \mathrm{d}S_0, \tag{17}$$

$$\frac{\partial^2 \Pi_h}{\partial \boldsymbol{\psi}_a \partial \boldsymbol{\psi}_b} = \sum_e^{\text{local}} \int_{\Omega_h^e} [\mathbf{C} : (\nabla_0 N_a \otimes \nabla_0 N_b)]\,\mathrm{d}V_0, \tag{18}$$

where a and b are node numbers, $\mathbf{P} = \partial W/\partial \mathbf{F}$ is the first Piola–Kirchhoff stress tensor and $\mathbf{C} = \partial^2 W/\partial \mathbf{F}^2$ is the Lagrangian tangent stiffness tensor. These quantities are the finite deformation analogs of the Cauchy stress and elastic modulus tensors familiar from linear elasticity. Note that in the first term of eqn. (17) and in eqn (18) e is only summed over *local* elements in B_0. Explicitly in indicial notation the above expressions can be rewritten as

$$\frac{\partial \Pi_h}{\partial \psi_a^i} = \sum_e^{\text{local}} \int_{\Omega_h^e} P_{iJ} N_{a,J}\,\mathrm{d}V_0 - \int_{B_0} \rho_o B_i N_a\,\mathrm{d}V_0 - \int_{\partial B_{02}} \bar{T}_i N_a\,\mathrm{d}S_0, \tag{19}$$

$$\frac{\partial^2 \Pi_h}{\partial \psi_a^i \partial \psi_b^k} = \sum_e^{\text{local}} \int_{\Omega_h^e} [C_{iJkL} N_{a,J} N_{b,L}]\,\mathrm{d}V_0, \tag{20}$$

and P_{iJ} and C_{iJkL} are related to strain energy density through

$$P_{iJ} = \frac{\partial W}{\partial F_{iJ}}, \tag{21}$$

$$C_{iJkL} = \frac{\partial^2 W}{\partial F_{iJ}\partial F_{kL}}. \tag{22}$$

These Lagrangian measures can be related to their spatial counterparts, the Kirchhoff stress τ and the spatial moduli **c** through the standard derivation (Marsden and Hughes 1983)

$$P_{iJ} = \tau_{ij} F_{Jj}^{-1}, \tag{23}$$

$$C_{iJkL} = (c_{ijkl} + \delta_{ik}\tau_{jl}) F_{Jj}^{-1} F_{Ll}^{-1}, \tag{24}$$

where δ_{ik} is the Kronecker delta. For the 3-noded linear element scheme adopted in this work, **F** is constant within each element; thus the integrations above amount to evaluating the integrand for the deformation gradient **F** within that element and multiplying by the element area.

So far our treatment has been totally general and applicable regardless of choice of underlying atomistic methodology. The appropriate relations for an EAM formulation are given below. In the previous discussion the EAM expressions (2)–(5) were given for an arbitrary collection of atoms and the energy computed by summation over all atoms. For a pure infinite crystal subjected to homogeneous deformation, translational invariance reduces the general expressions to consideration of a single atom and all neighbours within a prespecified cut-off radius r_c. Thus eqns. (3) and (5) may be rewritten as

$$\Phi = \frac{1}{2}\sum_{\mathbf{m}} \phi(r^{\mathbf{m}}), \tag{25}$$

$$\rho = \sum_{\mathbf{m}} f(r^{\mathbf{m}}), \tag{26}$$

where the indices $\mathbf{m} = (m_1, m_2, m_3)$ are summed over all atoms within the cut-off sphere of the representative atom after deformation, $\phi(r)$ is the interaction pair potential, $f(r)$ is the electron density function, and

$$r^{\mathbf{m}} = |\mathbf{x}(\mathbf{m})|. \tag{27}$$

The strain energy density of an infinite crystal undergoing homogeneous deformation is

$$W = \frac{1}{\Omega}[U(\rho) + \Phi], \tag{28}$$

where Ω is the unit cell volume.

Given the form of the total energy of the crystal (eqn. (28)), the local stresses and tangential elastic moduli can be derived at every point within the crystal. Differentiating eqn. (28) with respect to the deformation gradient components, we obtain the components of the first Piola–Kirchhoff stress tensor (eqn. (21))

$$P_{iJ} = \frac{1}{\Omega}\left[U'(\rho)\frac{\partial \rho}{\partial F_{iJ}} + \frac{\partial \Phi}{\partial F_{iJ}}\right]. \tag{29}$$

These derivatives may be evaluated through use of eqns (25) and (26) and by exploiting the identity

$$\frac{\partial r^{\mathbf{m}}}{\partial F_{iJ}} = \frac{r_i^{\mathbf{m}} r_j^{\mathbf{m}}}{r^{\mathbf{m}}} F_{Jj}^{-1}, \tag{30}$$

where

$$r_i^{\mathbf{m}} = x_i(\mathbf{m}). \tag{31}$$

As a result, it is found that

$$P_{iJ} = \frac{1}{\Omega}\sum_{\mathbf{m}}\left\{\left[U'(\rho)f'(r^{\mathbf{m}}) + \frac{1}{2}\Phi'(r^{\mathbf{m}})\right]\frac{r_i^{\mathbf{m}} r_j^{\mathbf{m}}}{r^{\mathbf{m}}}\right\}F_{Jj}^{-1}. \tag{32}$$

The Kirchhoff stress τ_{ij} follows by eqn. (23) as

$$\tau_{ij} = \frac{1}{\Omega}\sum_{\mathbf{m}}\left\{\left[U'(\rho)f'(r^{\mathbf{m}}) + \frac{1}{2}\Phi'(r^{\mathbf{m}})\right]\frac{r_i^{\mathbf{m}} r_j^{\mathbf{m}}}{r^{\mathbf{m}}}\right\}. \tag{33}$$

We now turn to the Lagrangian tangential moduli defined in eqn. (22). Making use of eqns (25) and (26) as before we have

$$\begin{aligned} C_{iJkL} = \frac{1}{\Omega}\Bigg\{ & U''(\rho)\left[\sum_{\mathbf{m}} f'(r^{\mathbf{m}})\frac{\partial r^{\mathbf{m}}}{\partial F_{iJ}}\right]\left[\sum_{\mathbf{n}} f'(r^{\mathbf{n}})\frac{\partial r^{\mathbf{n}}}{\partial F_{kL}}\right] \\ & + \sum_{\mathbf{m}}\Bigg[\left(U'(\rho)f''(r^{\mathbf{m}}) + \frac{1}{2}\phi''(r^{\mathbf{m}})\right)\frac{\partial r^{\mathbf{m}}}{\partial F_{iJ}}\frac{\partial r^{\mathbf{m}}}{\partial F_{kL}} \\ & + \left(U'(\rho)f'(r^{\mathbf{m}}) + \frac{1}{2}\phi'(r^{\mathbf{m}})\right)\frac{\partial^2 r^{\mathbf{m}}}{\partial F_{iJ}\partial F_{kL}}\Bigg]\Bigg\}. \end{aligned} \tag{34}$$

The partial derivatives appearing in eqn. (34) are geometrical identities and are given in eqn. (30) and below,

$$\frac{\partial^2 r^{\mathbf{m}}}{\partial F_{iJ}\partial F_{kL}} = \frac{[\delta_{ik}(r^{\mathbf{m}})^2 - r_i^{\mathbf{m}} r_k^{\mathbf{m}}] r_j^{\mathbf{m}} r_l^{\mathbf{m}}}{(r^{\mathbf{m}})^3} F_{Jj}^{-1} F_{Ll}^{-1}. \tag{35}$$

The spatial moduli are then obtained by recalling eqn. (24),

$$\begin{aligned} c_{ijkl} = \frac{1}{\Omega}\Bigg\{ & U''(\rho)\left[\sum_{\mathbf{m}} f'(r^{\mathbf{m}})\frac{r_i^{\mathbf{m}} r_j^{\mathbf{m}}}{r^{\mathbf{m}}}\right]\left[\sum_{\mathbf{n}} f'(r^{\mathbf{n}})\frac{r_k^{\mathbf{n}} r_l^{\mathbf{n}}}{r^{\mathbf{n}}}\right] \\ & + \sum_{\mathbf{m}}\Bigg[\left(\left(U'(\rho)f''(r^{\mathbf{m}}) + \frac{1}{2}\phi''(r^{\mathbf{m}})\right) - \frac{1}{r^{\mathbf{m}}}\left(U'(\rho)f'(r^{\mathbf{m}}) + \frac{1}{2}\phi'(r^{\mathbf{m}})\right)\right) \\ & \frac{r_i^{\mathbf{m}} r_j^{\mathbf{m}} r_k^{\mathbf{m}} r_l^{\mathbf{m}}}{(r^{\mathbf{m}})^2}\Bigg]\Bigg\}. \end{aligned} \tag{36}$$

Note that the Kronecker delta term appearing in eqn. (35) drops out due to the presence of the stress term in eqn. (24).

For a purely local formulation the above expressions represent a complete constitutive description of the problem. However, as explained earlier, a purely local formulation is unable to capture non-uniform effects such as stacking faults, interfaces and free surfaces. The non-local formulation is developed below.

2.5. *Non-local quasicontinuum*

In the non-local formulation each quadrature point is represented by a single atom whose neighbours are displaced in accordance with the continuum displacement fields (see fig. 5). Due to the inhomogeneous nature of the non-local formulation the global lattice origin is retained and we must explicitly account for the position of the atoms in the representative crystallite in relation to the continuum mesh. We thus introduce $\mathbf{R}^e$ as the global cartesian coordinates of the representative atom of element e and write the positions of the atoms belonging to its representative crystallite as

$$\mathbf{X}^e(\mathbf{m}) = \mathbf{R}^e + m_I \mathbf{A}_I, \quad \mathbf{m} \in Z^3. \tag{37}$$

In this way the Bravais lattice is tied to the mesh, and a one-to-one relationship between the atomic sites and continuum fields is obtained. The deformed atomic positions are obtained by interpolation from the FEM mesh,

$$\mathbf{x}^{\mathrm{e}}(\mathbf{m}) = \mathbf{X}^{\mathrm{e}}(\mathbf{m}) + \psi_a N_a(\mathbf{X}^{\mathrm{e}}(\mathbf{m})). \tag{38}$$

In the non-local case, due to the absence of a uniform strain field, it is not possible to define general measures of stress and stiffness as in the local case. As a result, the out-of-balance force residual and global stiffness must be written directly in terms of the EAM sums. The non-local contribution to the out-of-balance force residual follows as

$$\frac{\partial \Pi_h}{\partial \psi_a^i} = \sum_e^{\text{non-local}} \left\{ \frac{1}{\Omega} \sum_{\mathbf{m}} \left[\left(U'(\rho_e) f'(r_e^{\mathbf{m}}) + \frac{1}{2}\phi'(r_e^{\mathbf{m}}) \right) \frac{\partial r_e^{\mathbf{m}}}{\partial \psi_a^i} \right] \Omega_h^e \right\}, \tag{39}$$

where e is only summed over non-local elements in B_0, Ω_h^e is the area of element e, and the electron density at the representative atom of element e, ρ_e, is given by

$$\rho_e = \sum_{\mathbf{m}} f(r_e^{\mathbf{m}}), \tag{40}$$

where

$$\begin{aligned} r_e^{\mathbf{m}} &= |\mathbf{x}^e(\mathbf{m}) - \mathbf{x}^e(\mathbf{0})|, \\ &= |m_I \mathbf{A}_I + \psi_a (N_a(\mathbf{X}^{\mathrm{e}}(\mathbf{m})) - N_a(\mathbf{R}^{\mathrm{e}}))|. \end{aligned} \tag{41}$$

The partial derivative appearing in eqn. (39) is a geometric identity and is given by

$$\frac{\partial r_e^{\mathbf{m}}}{\partial \psi_a^i} = (N_a(\mathbf{X}^e(\mathbf{m})) - N_a(\mathbf{R}^{\mathrm{e}})) \frac{(r_i^{\mathbf{m}})_e}{r_e^{\mathbf{m}}}, \tag{42}$$

where

$$(r_i^{\mathbf{m}})_e = x_i^e(\mathbf{m}) - x_i^e(\mathbf{0}). \tag{43}$$

Note that for FEM meshes containing both local and non-local elements, the total out-of-balance force residual $\partial \Pi_h / \partial \psi_a$ will be assembled from both eqns (19) and (39) as a superposition of both vectors. The non-local contribution to the global stiffness matrix can similarly be obtained:

$$\begin{aligned} \frac{\partial^2 \Pi_h}{\partial \psi_a^i \partial \psi_b^j} = \sum_e^{\text{non-local}} \frac{1}{\Omega} \Bigg\{ & U''(\rho_e) \left[\sum_{\mathbf{m}} f'(r_e^{\mathbf{m}}) \frac{\partial r_e^{\mathbf{m}}}{\partial \psi_a^i} \right] \left[\sum_{\mathbf{n}} f'(r_e^{\mathbf{n}}) \frac{\partial r_e^{\mathbf{n}}}{\partial \psi_b^j} \right] \\ & + \sum_{\mathbf{m}} \left[\left(U'(\rho_e) f''(r_e^{\mathbf{m}}) + \frac{1}{2}\phi''(r_e^{\mathbf{m}}) \right) \frac{\partial r_e^{\mathbf{m}}}{\partial \psi_a^i} \frac{\partial r_e^{\mathbf{m}}}{\partial \psi_b^j} \right. \\ & \left. + \left(U'(\rho_e) f'(r_e^{\mathbf{m}}) + \frac{1}{2}\phi'(r_e^{\mathbf{m}}) \right) \frac{\partial^2 r_e^{\mathbf{m}}}{\partial \psi_a^i \partial \psi_b^j} \right] \Bigg\}, \end{aligned} \tag{44}$$

where eqn. (42) is used in addition to identity

$$\frac{\partial^2 r_e^{\mathbf{m}}}{\partial \psi_a^i \partial \psi_b^j} = (N_a(\mathbf{X}^e(\mathbf{m})) - N_a(\mathbf{R}^e))(N_b(\mathbf{X}^e(\mathbf{m})) - N_b(\mathbf{R}^e)) \frac{\delta_{ij}(r_e^{\mathbf{m}})^2 - (r_i^{\mathbf{m}})_e (r_j^{\mathbf{m}})_e}{(r_e^{\mathbf{m}})^3}. \tag{45}$$

Again, meshes containing both local and non-local elements yield a final stiffness matrix that is obtained by superposition of both eqns (20) and (44). The inclusion of

non-local elements near highly deformed regions such as defect cores, stacking faults, and free surfaces completes the QC formulation.

2.6. *Non-locality criterion*

As explained above, one of the key ingredients in the QC formulation is the placement of non-local elements in highly deformed regions. In this section we introduce a criterion for determining the local vs. non-local status of each element in the mesh. A natural choice suggested by figs 4 and 5 is a size-dependent criterion; elements larger than the local crystallite radius R_c could be computed locally, while smaller elements could receive non-local treatment. While this criterion makes sound physical sense and leads to excellent solutions, it proves to be wasteful from a computational point of view.

The non-local capabilities of the QC formulation are only needed close to defect cores and along slip planes where stacking faults develop. Once away from these highly non-homogeneous regions the local formulation (which is less computationally intensive and more stable) performs remarkably well. Therefore it is of interest to develop a criterion capable of identifying regions undergoing large non-homogeneous deformation.

The criterion used in subsequent sections is based on the second invariant of the Lagrangian strain tensor $\mathbf{E}$

$$\begin{aligned} II_E &= \tfrac{1}{2}[\mathbf{E} : \mathbf{E} - (\mathrm{tr}\mathbf{E})^2], \\ &= E_{12}^2 + E_{13}^2 + E_{23}^2 - (E_{11}E_{22} + E_{22}E_{33} + E_{11}E_{33}), \end{aligned} \tag{46}$$

where

$$\mathbf{E} = \tfrac{1}{2}(\mathbf{F}^{\mathrm{T}}\mathbf{F} - \mathbf{I}). \tag{47}$$

According to our criterion, an element is given non-local status when

$$\sqrt{|II_E|} > \epsilon_{\mathrm{cr}}, \tag{48}$$

where ϵ_{cr} is some critical strain appropriate to the material and problem. In addition to the elements that satisfy condition (48) outright, we also demand that elements in their immediate vicinity that share atoms with those elements determined to be non-local by the strain criterion be treated as non-local as well. These additional elements are referred to as non-local by proximity.

This leaves one further consideration. Consider, for example, a model containing a dislocation as in fig. 8 (only elements along the slip plane have been indicated in the figure). Elements far to the right of the dislocation core will be undistorted, while elements far to the left experience perfect Burgers vector slip. In both cases these are zero energy modes corresponding to a perfect undistorted crystal and can be treated using local elements. However, with the purely kinematical criterion (48) introduced so far, the elements on the far left of the slip plane are identified as non-local.

As a result, a more stringent non-locality criterion is added to the kinematic criterion described above, namely in addition to being highly strained the deformation within the element should imply a non-zero strain energy

$$W_h^e > W_{\mathrm{tol}}, \tag{49}$$

where W_{tol} is some small number. To summarize, the procedure for determining the status of all elements in the mesh is as follows:

Fig. 8

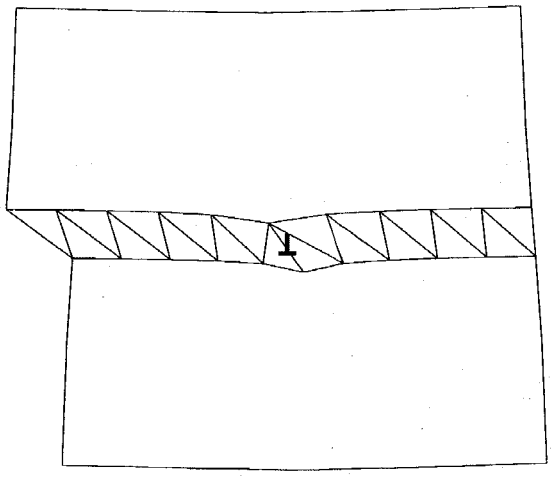

Slip plane elements near a dislocation core.

(i) Compute the Lagrangian strain tensor for all elements in the mesh.
(ii) Check condition (48) for all elements smaller than R_c, identifying non-locally strained elements.
(iii) Compute the energy of elements identified in (ii) using the non-local formulation of the model, and retain those elements satisfying eqn. (49) as non-local.
(iv) Locate elements that are non-local by proximity by identifying all elements smaller than R_c that are within R_c of an element satisfying both eqns (48) and (49).
(v) In addition, all surface and interfacial elements are computed non-locally.

This procedure is carried out at the start of each iteration and is integrated into the solution process so that no computation time is lost. An important caveat regarding this algorithm is that to ensure convergence once an element is labelled as non-local it must remain so from that point on even if in future iterations it no longer satisfies the non-locality criterion or is no longer in proximity to a non-local element. As an example, fig. 9 presents a colour-coded plot of the elements near the core of a dislocation. The red elements near the centre are those satisfying both parts of the non-locality criterion and are thus fully non-local. The dark blue elements along the slip plane only satisfy eqn. (48) and are thus kinematically non-local. These elements are computed using the non-local scheme but do not trigger additional non-local elements in their vicinity. The green elements are non-local by proximity to the fully non-local elements, and the yellow elements in the rest of the model are local. In this manner the important nonlinear effects near the core are captured while the rest of the model is treated using the local algorithm.

§ 3. Some test cases: dislocations in fcc crystals

It is instructive to probe the limiting behaviour of the theory on the atomistic scale. Here the question is whether the theory can stably support lattice defects such as dislocations and, if so, how similar are their core structures to those predicted by a full atomistic simulation. Three fcc configurations were investigated: stacking faults

Fig. 9

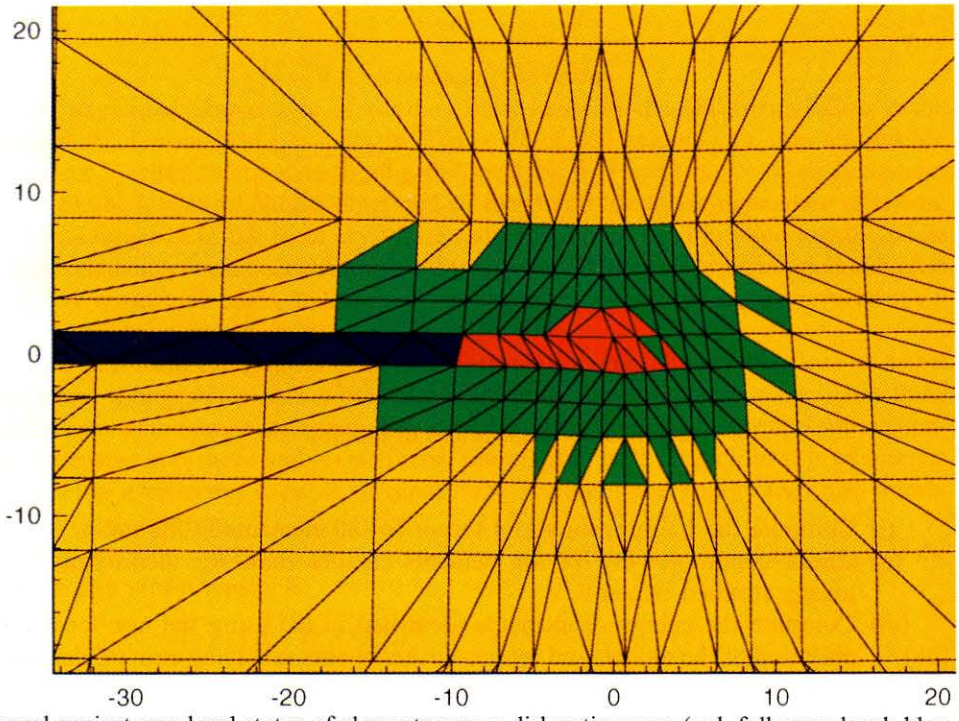

Local against non-local status of elements near a dislocation core (red, fully non-local; blue, kinematically non-local; green, non-local by proximity; yellow, local).

within the (111) plane, the Lomer edge dislocation $(001)[1\bar{1}0]$ and the primary fcc edge dislocation $(111)[\bar{1}10]$. In all cases the method was shown to be in very good agreement with the lattice statics results under conditions in which the same potentials were used in addition to equivalent boundary conditions. In the following examples the constitutive behaviour of the crystal is modelled using the EAM potentials for aluminium due to Ercolessi and Adams (1993) with a cut-off radius (r_c) of 5·56 Å. The lattice parameter (a_0) is 4·032 Å. We chose a representative crystallite radius (R_c) of 9·87 Å which for the perfect fcc lattice corresponds to 12 neighbour shells containing 249 atoms. The critical non-local strain (ϵ_{cr}) used in the non-locality criterion is 10% and the zero energy tolerance (W_{tol}) is 10^{-3} eV Å^{-3}.

3.1. *Stacking faults*

An important feature of the QC/FEM formulation is its capacity to model the type of stacking faults (SFs) that often arise in crystalline deformation processes. In fcc crystals, stacking faults are known to form on the dominant $\{111\}\langle 110\rangle$ slip system, for example, as a result of dissociation of a perfect edge dislocation into two Shockley partial dislocations via the reaction

$$\tfrac{1}{2}[\bar{1}10] \rightarrow \tfrac{1}{6}[\bar{2}11] + \tfrac{1}{6}[\bar{1}2\bar{1}]. \tag{50}$$

The two partials can then drift apart leaving a stacking fault ribbon between them. Due to the imperfect stacking sequence in this ribbon there is an energy penalty

associated with its presence (i.e. the SF energy), which acts to limit the indefinite drift of the partials (this will be investigated more thoroughly in § 3.3). The expected out-of-plane displacement jump across the stacking fault plane is $\sqrt{6}a_0/12$. For aluminium this is 0·823 Å.

We begin by computing the SF energy directly from a lattice statics (LS) computation. The unrelaxed SF energy resulting from the use of the Ercolessi–Adams potentials is 7·530 meV Å^{-2}. From the LS computation it is found that the atoms on each of the four (111) planes adjacent to the slip plane (two above and two below) contribute equally to the SF energy. This information is instructive in the construction of the FEM mesh. On relaxation, the SF energy is reduced to about 6·5 meV Å^{-2} (Ercolessi and Admas 1993). This value compares reasonably with the observed experimental values for aluminium of 7·5–9 meV Å^{-2}.

We now turn to the QC/FEM solution for the SF problem. Two different analyses were carried out. In the first the FEM model was created in the plane containing the stacking fault. The x direction was taken to coincide with the Shockley partial direction $[\bar{2}11]$, and the y direction was set to the slip plane normal [111]. The initial slip was introduced into the model by moving all nodes above the slip plane to the right by the magnitude of the Shockley partial $a_0/\sqrt{6}$, and then constraining all boundary nodes to their initial positions. The initially displaced mesh is presented in fig. 10. The mesh contains 42 elements and 32 nodes for a total of 36 unconstrained degrees of freedom.

Two different elements are present in the mesh: large nearly equilateral elements, and long narrow elements. The equilateral elements are larger than R_c and are thus local; the long narrow elements are non-local, but because their width is larger than

Fig. 10

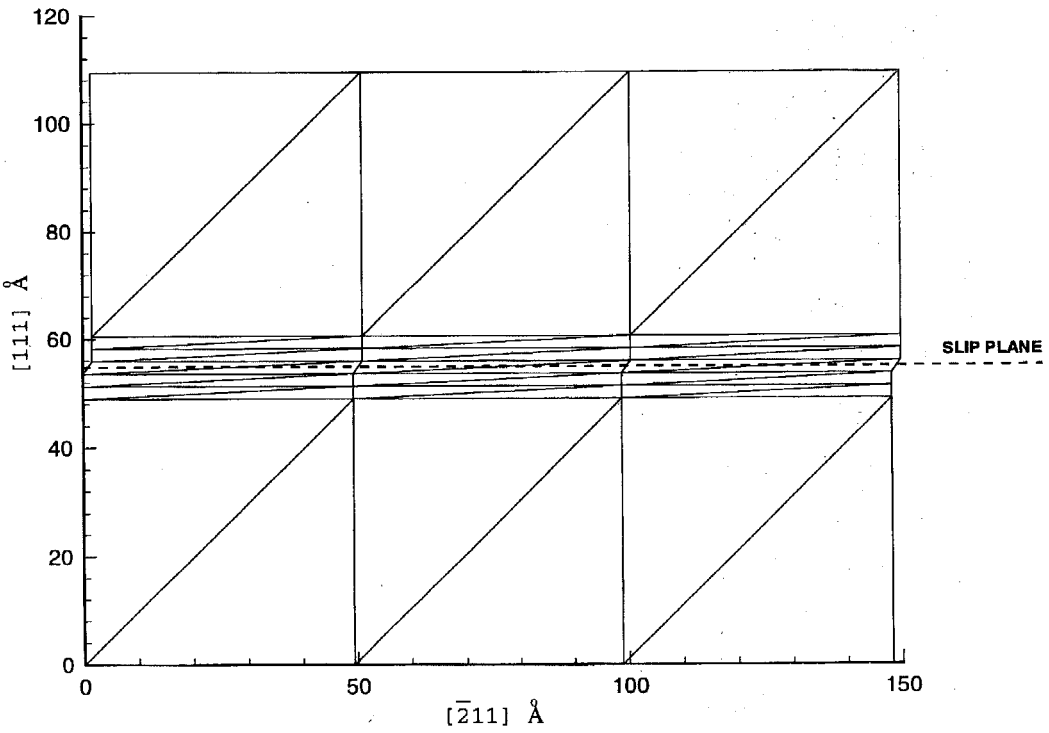

Initially distorted stacking fault FEM mesh.

R_c, these elements only exhibit non-local effects in the y direction. In this manner surface effects are eliminated from the model. The height of the narrow elements is set exactly equal to the interplanar distance in the (111) direction $a_0/\sqrt{3}$, and the global origin is selected such that these elements fall between adjacent atomic planes (see fig. 11 (*a*)). This allows the elements straddling the slip plane to act as a kinemtical mechanism for introducing slip. Thus from the atomistic point of view there is a jump in displacement across the slip plane as expected, while in the continuum we see a continuous linear variation in slip. Since the energy is computed atomistically, the manner in which the slip is distributed in the continuum is inconsequential. Five layers of the narrow elements are necessary to capture the contributions of the four atomic planes adjacent to the slip plane to the SF energy (see fig. 11 (*b*)), as explained above. The SF energy associated with the model is equal to the total energy per unit thickness divided by the width of the model.

The unrelaxed SF energy obtained from this model is identical to that obtained from the LS analysis. Following NR minimization we find a relaxed SF energy of about 6·2 meV Å^{-2}, smaller than the LS value, but comparable.

In the second analysis the FEM model was created in the primary [$\bar{1}$10]–[111] coordinate system and a deformation corresponding to a 1/2 Burgers vector slip was

Fig. 11

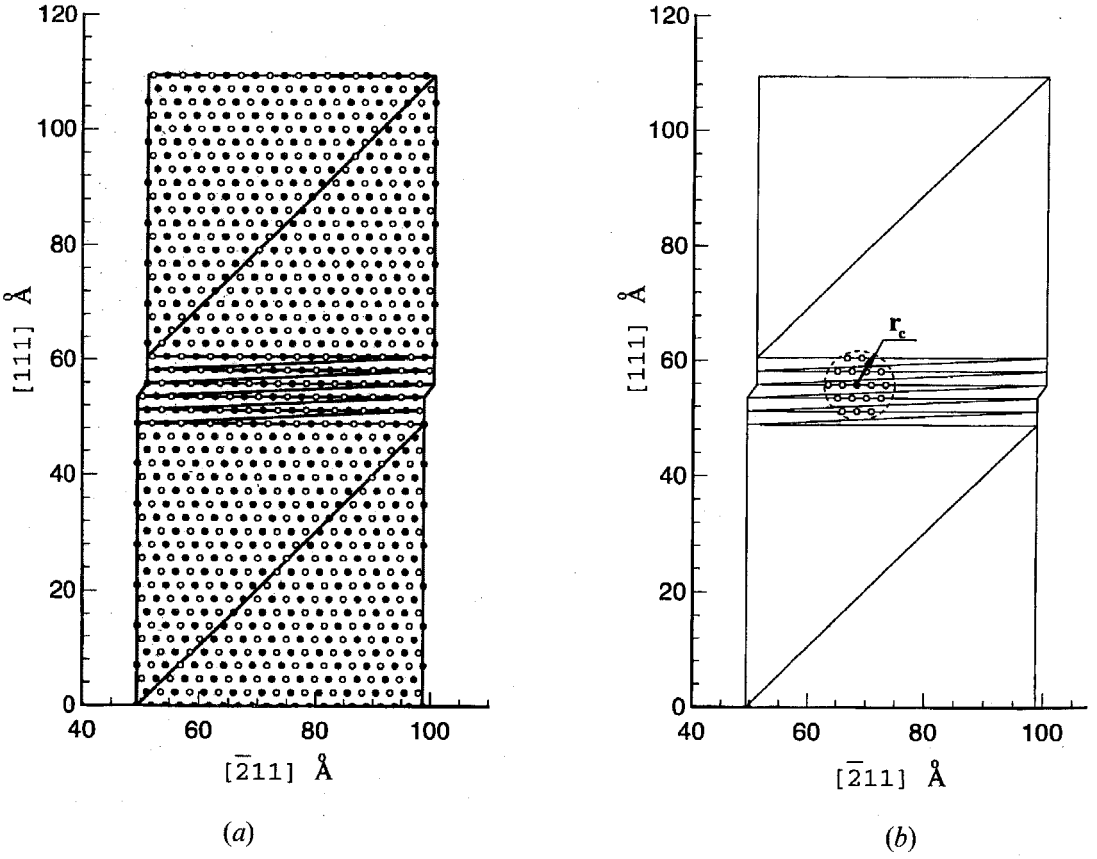

Central elements of SF mesh. (*a*) Underlying crystal structure superimposed on elements. Shading of atoms indicates depth (black = 0 Å, white = 1·426 Å). (*b*) Representative atom (black) of central slip element surrounded by all atoms within its cut-off radius.

introduced. On relaxation the SF energy was found to be the same as in the previous Shockley partial analysis, and out-of-plane displacements between 0·822 and 0·824 Å were observed in all nodes above the slip plane, very close to the expected value.

3.2. *Lomer dislocation*

The Lomer dislocation is generated at high temperatures by the interesection of two extended $\langle 110 \rangle$ edge dislocations gliding on separate $\{111\}$ planes. The Shockley partials of these dislocations react to form the $\{001\}\langle 110 \rangle$ Lomer dislocation. As both the Burger's vector and dislocation line of this system lie in the $\{100\}$ plane, which is not an fcc glide plane, the dislocation tends to be sessile and acts as a barrier to dislocation glide on the two intersecting $\{111\}$ planes. Solving the problem using both the LS approach and the QC approach results in a stable core for the Lomer dislocation. The structures obtained using both methods are nearly identical.

In the LS approach a cylinder of atoms is displaced according to the linear elastic solution for a straight dislocation in an anisotropic medium as given in Hirth and Lothe (1992). One important question that arises here and also in the QC model described later is where to place the singular elastic core with respect to the discrete atomic positions. By moving the singularity associated with the elastic solution with respect to the underlying crystal lattice, slightly different initial conditions are generated, though all are found to converge to the same final core structure.

Periodic boundary conditions are applied in the out-of-plane $[\bar{1}\bar{1}0]$ direction, and an outer annulus of atoms is frozen in correspondence with the elasticity solution. We then allow the unconstrained atoms to relax into equilibrium positions by minimizing the total potential energy using a CG method. Once the energy is fully minimized a small random displacement is applied to the atoms near the core and the minimization process is restarted to ensure that a stable minimum has been reached. The final relaxed core structure and slip distribution plot are given in fig. 16 (*a*). Note the highly symmetrical pentagonal structure obtained. A typical LS run for this type of problem contains between 50 000 and 100 000 degrees of freedom.

In the QC approach we begin, as before, by defining a FEM mesh. The x direction is taken to coincide with the slip direction $[1\bar{1}0]$, and the y direction is set to the slip plane normal [001]. All nodes in the mesh are then displaced according to the same anisotropic elasticity solution referred to above in the LS case and displacement boundary conditions are applied (i.e. the displacements of all nodes on the model boundaries are frozen to the elasticity solution values). In addition, all out-of-plane displacements are constrained to zero to force plane strain conditions (this is equivalent to the periodic BCs along the line direction applied in the LS analysis). The initial distorted mesh appears in fig. 12 (*a*) and a colour-coded representation of the same mesh indicating the local/non-local status of the elements near the dislocation core was given previously in fig. 9 and discussed in § 2.6. Note the refinement near the core where anharmonic effects are expected and the gradual coarsening of the mesh away from it.

As in the SF mesh discussed in the previous section the element size is kept larger than R_c near the model boundaries to eliminate surface effects, thus allowing us to model a dislocation in an infinite crystal. Also, as in the SF mesh a ribbon of five elements with a height equal to the interplanar spacing in the y direction ($a_0/2$ for this orientation) is included to correctly capture stacking fault effects in case the Lomer dissociates, and to kinematically introduce the slip. The mesh contains 700

Fig. 12

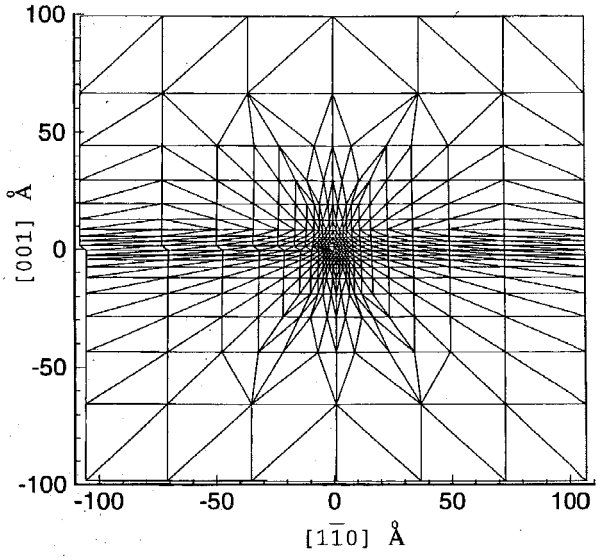

(*a*)

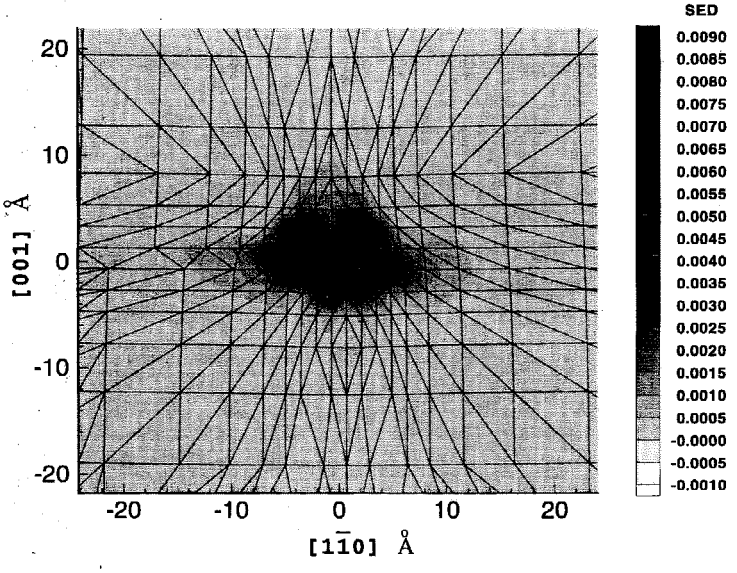

(*b*)

Lomer dislocation QC model. (*a*) Initially distorted FEM mesh. (*b*) Close-up of Lomer core and initial strain energy density (eV Å^{-2}).

elements and 376 nodes for a total of 568 unconstrained degrees of freedom (significantly less than the LS analysis).

Figure 12 (*b*) shows the initial strain energy density (SED) associated with the linear elasticity trial solution near the core. One significant aspect of this plot is that the slip ribbon elements are energy-free, indicating that the model is capable of supporting stable defects. As noted earlier, this effect is a direct reflection of the lack of convexity of the energy functional. By way of contrast, fig. 13 shows the initial strain energy that would be associated with a linear elastic constitutive model, indicating again the crucial role of the slip invariance described above. Here the

Fig. 13

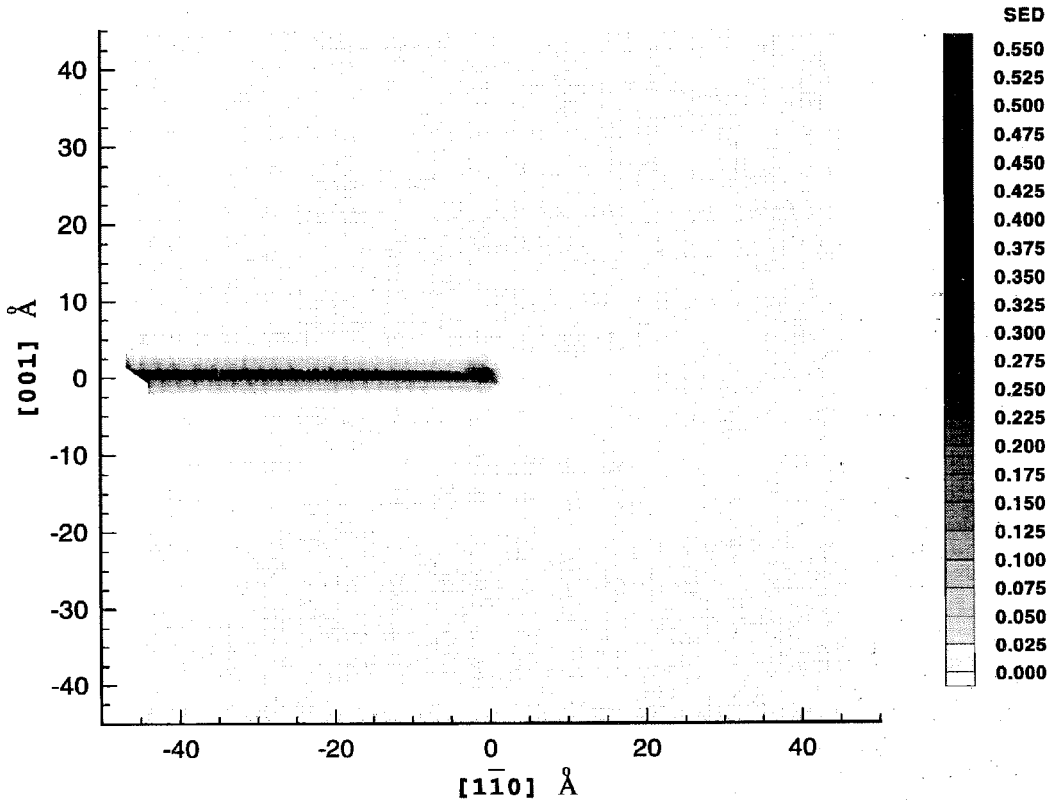

Initial elastic strain energy density (eV Å^{-2}) associated with a Lomer dislocation as obtained using a linear elastic constitutive model.

convexity of the strain energy leads to an energy penalty for fully slipped elements on the slip plane.

CG minimization of the total potential energy leads to a relaxed SED such as is shown in fig. 14. Comparing with fig. 12(*b*) we see a reduction in the strain energy density near the core from 0·0087 to 0·0067 eV Å^{-2}. The fact that the energy remains concentrated near the core indicates that the dislocation remains undissociated.

Figure 15 contains the relaxed continuum displacement fields. An alternative representation of these fields is obtained by displacing the atoms of the underlying crystal, uniquely tied to the continuum through the global crystal origin, according to the displacement at their coordinates. When this is done and the results compared with the LS structure we see very good agreement between the methods (fig. 16(*a*)) with maximum deviations near the core of between 0·1–0·2 Å. Figure 16(*b*) shows the displacement jump across the slip plane in the x-direction (slip) and the y-direction (opening displacement). The QC solution is less smooth than the LS solution due to the reduction in the number of degrees of freedom; however, the agreement between the methods is good, and significantly, both predict the same core size.

Re-examining the SED plot (fig. 14) we find regions exhibiting a negative energy (relative to the crystal cohesive energy). This goes back to the discussion of non-centrosymmetry effects presented in § 2.1. It is instructive to compare the atomic neighbour structure of an atom in the QC model which is found to have a negative

Fig. 14

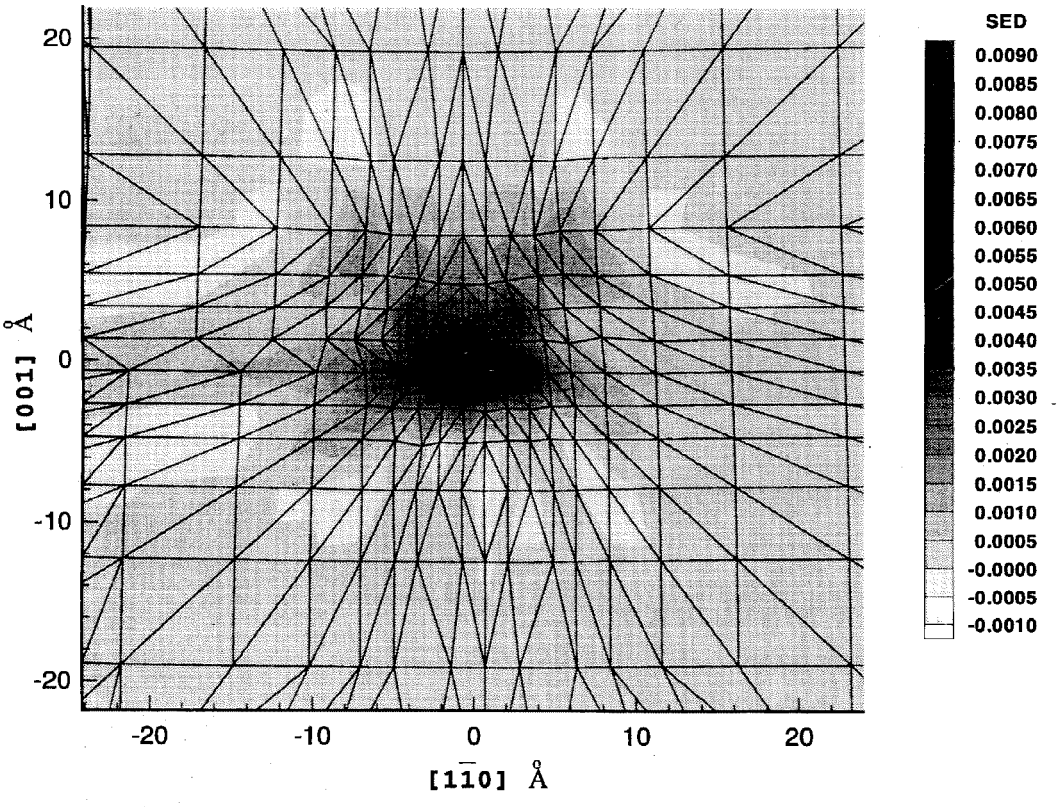

Relaxed QC Lomer dislocation strain energy density (eV Å^{-2}).

energy with the identical atom in the LS analysis where all atoms have positive energy. This is presented in fig. 17. The investigated atom (indicated in the figure) has 42 neighbours within the potential cutoff radius. The distance of each neighbour from the investigated atom is plotted. It is interesting to see that the differences are very small (less than 0·1 Å), strengthening our earlier conclusion that these effects are small and can be neglected.

3.3. *Edge dislocation*

As a final example we investigate the primary $\{111\}\langle 110\rangle$ edge dislocation. As explained in § 3.1 this dislocation often dissociates into an extended dislocation composed of two Shockley partial dislocations delimiting a stacking fault ribbon.

The LS solution follows along the same lines as those presented in the previous section for the Lomer dislocation. We begin by displacing the atoms according to the anisotropic linear elastic solution for a perfect edge dislocation (fig. 18) and then use CG minimization to find the relaxed configuration. As expected, the dislocation dissociates and a final splitting distance of 15·4 Å is observed (fig. 19). The atoms above and below the slip plane between the two partials move in opposite out-of-plane directions. The maximum out-of-plane displacement difference is observed midway between the partials and equals 0·643 Å. This value is less than the expected value of 0·823 Å, probably because of the small splitting distance allowing insufficient room for a fully developed SF to form. Figure 20 contains a SED plot generated directly from the LS solution (the energy of each atom is divided by the volume

Fig. 15

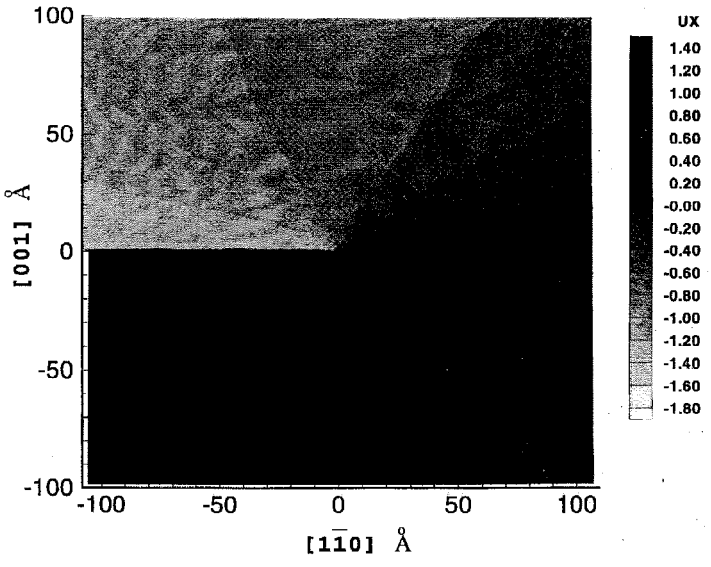

(*a*)

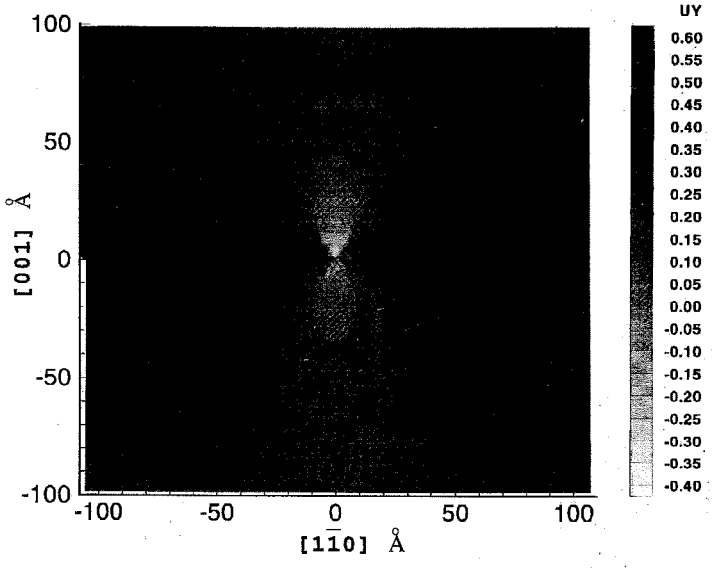

(*b*)

Relaxed QC Lomer dislocation displacement field, (*a*) u_x (Å), (*b*) u_y (Å).

of its Voronoi polyhedron to yield a strain energy density). The dissociated structure is clear.

The initial displaced QC mesh and SED plot are presented in fig. 21. The mesh has 1020 elements and 540 nodes, resulting in a total of 1332 degrees of freedoms. Figure 22 shows a plot of the representative atoms used in evaluating the constitutive input superimposed on the underlying crystal lattice. This plot demonstrates how the reduction in degrees of freedom in the QC method is achieved. Near the core all atoms are sampled and the QC formulation essentially reduces to straightforward LS, while away from the core fewer and fewer atoms are sampled as the solution tends to the linear elastic regime.

Fig. 16

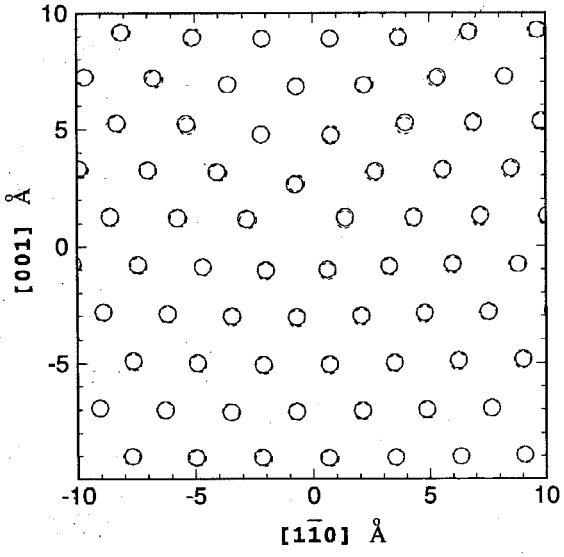

(*a*)

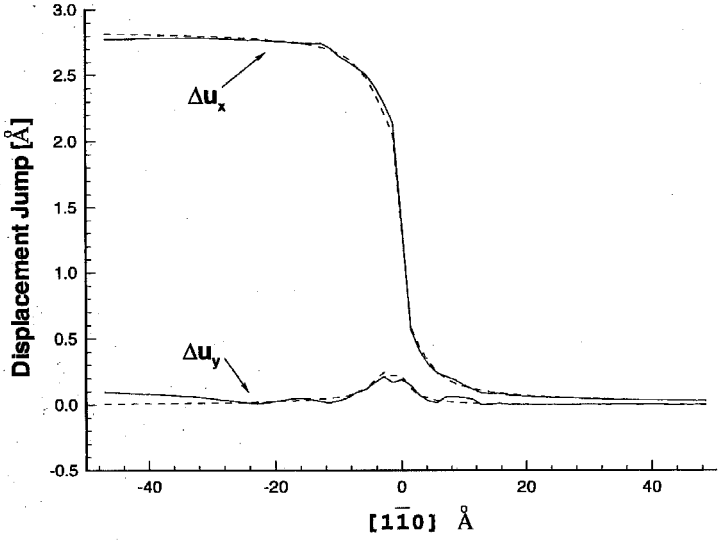

(*b*)

Comparison of LS(– – –) and QC (——) relaxed Lomer dislocation cores. (*a*) Atomic positions, (*b*) displacement jump across slip plane (Δu_x = slip, Δu_y = opening displacement).

Figure 23 presents the final relaxed SED plot. Comparing with the identical LS plot (fig. 20) we see that the overall magnitude and structure are similar but the QC picture is more noisy and again negative energies are encountered. However, despite the differences in the energy picture the final atomic structure is in excellent agreement with the LS structure and appears essentially identical to the LS solution presented previously in fig. 19. The relaxed out-of-plane displacement contour plot is presented in fig. 24, with a maximum displacement difference across the slip plane of 0·647 Å at the centre of the SF ribbon. Finally, fig. 25 presents the three components of the displacement jump across the slip plane (slip, opening

Fig. 17

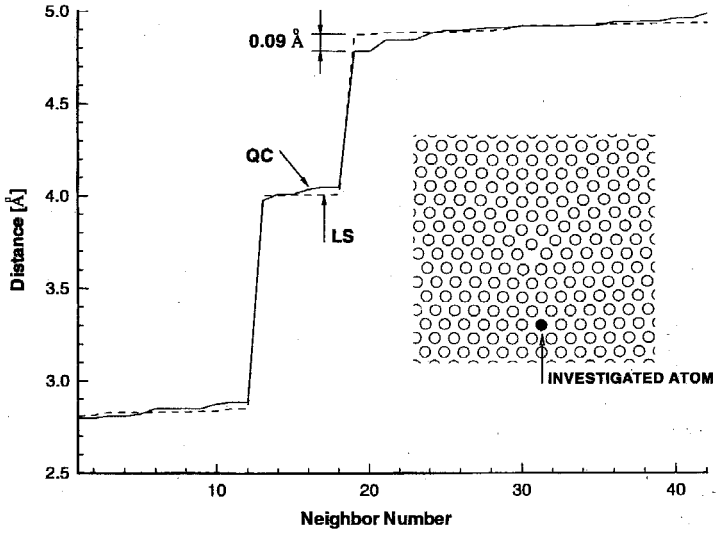

Atomic neighbourhood of an atom exhibiting negative energy in the QC Lomer solution compared with the neighbourhood of the same atom in the LS solution.

Fig. 18

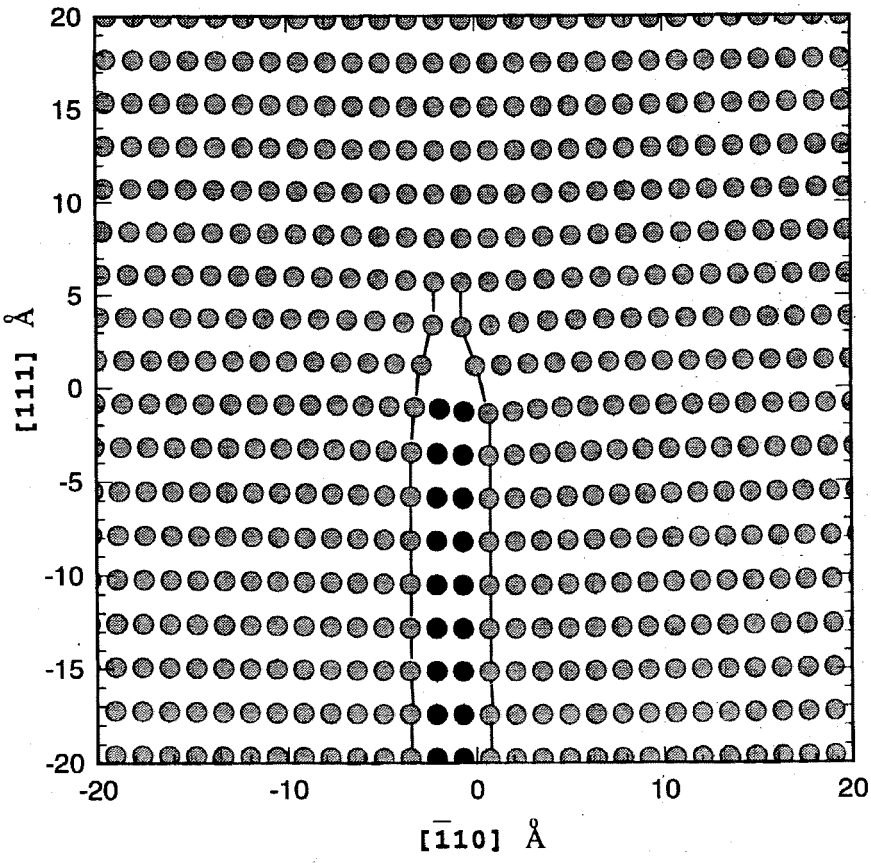

Initial atomic structure for the primary edge dislocation obtained from anisotropic linear elasticity.

Fig. 19

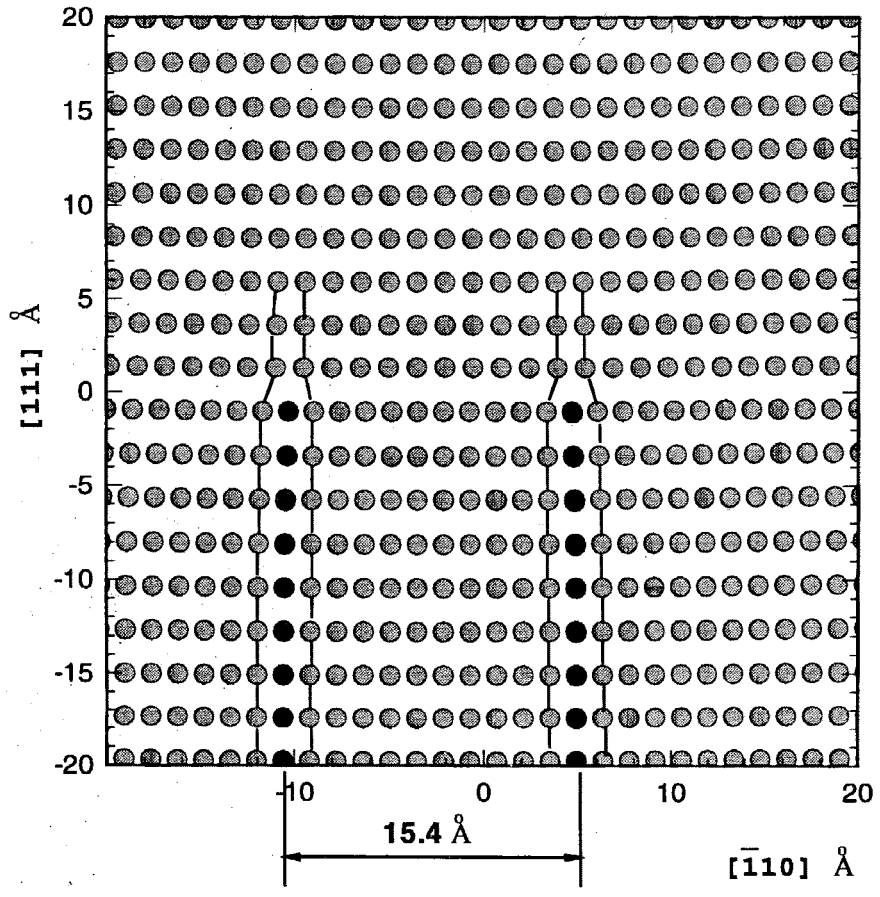

Final relaxed primary edge dislocation core (LS solution).

displacement and out-of-plane displacement) compared with the LS values. As in the Lomer case we find very good agreement between the two methods.

§ 4. Summary and conclusions

We have developed a method for the analysis of coupled atomistic/continuum deformation processes in crystals based on (i) the use of atomistic energy functions to describe the constitutive response of the material and (ii) the use of an adaptive finite element method for spanning multiple scales in the solution. The quasicontinuum theory thus derived permits the analysis of crystals directly from the underlying atomistic description of the total energy. In this manner, we can tap into the extensive repository of energy functions which has been developed in recent years, both from *ab-initio* calculations or by phenomenological approaches. The use of atomistic constitutive models also confers on the strain energy density of the solid a periodic structure. This in turn vastly enriches the range of possible behaviours of the solid by enabling the displacement field to develop structure on the scale of the lattice.

The atomistic limit of the theory has been tested by way of three examples: a stacking fault, a Lomer edge dislocation and a (111) edge dislocation in Al. While this is not the intended use of the theory—the analysis of a *single* defect core is performed far more effectively by a direct atomistic simulation—it is however important that reasonably accurate results be returned by the theory in this limit as well. It

Fig. 20

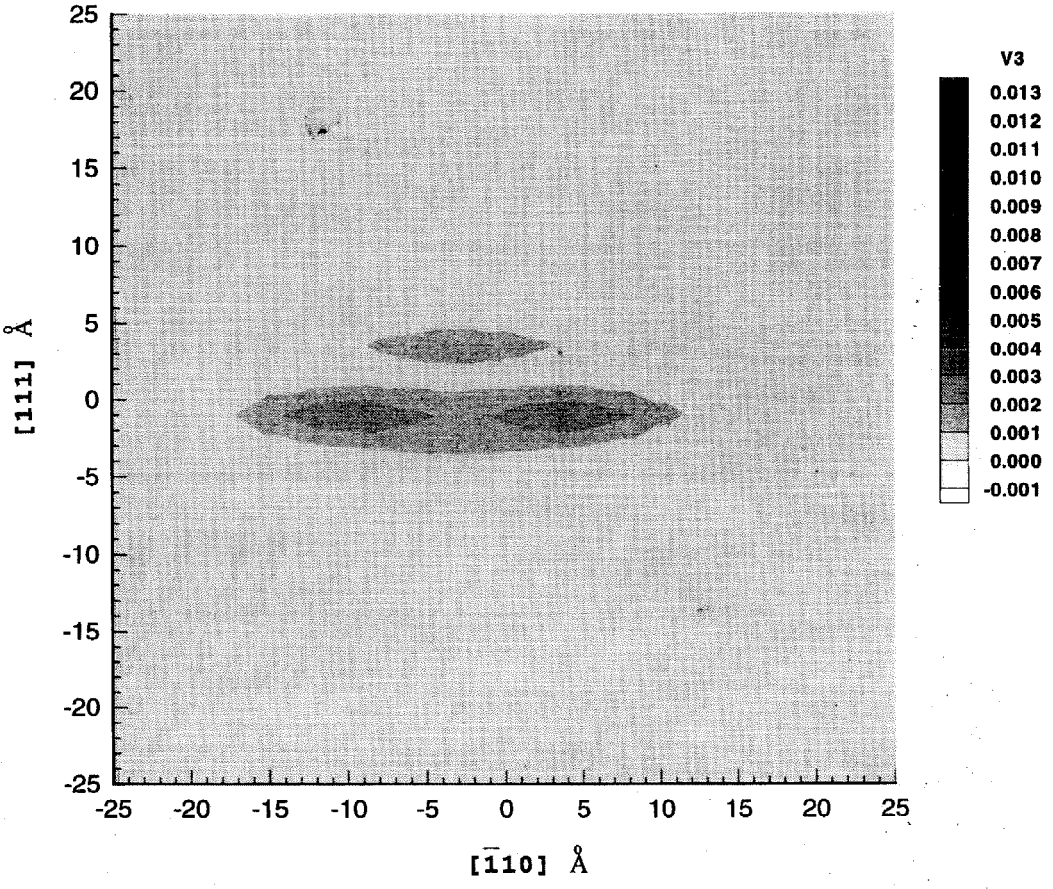

Relaxed primary edge dislocation (LS solution), strain energy density (eV Å^{-2}) near core.

is, therefore, satisfying that the predictions of the method are in excellent agreement with direct LS analysis in all three test cases considered. In the SF example, the unrelaxed SF energy is identical to the LS value, while the relaxed values are reasonably close. For the Lomer dislocation, both QC and LS predict a stable undissociated core and are in very good agreement vis-à-vis the final core structure. Finally in the (111) edge problem, both methods predict a relaxed dissociated structure with an identical splitting distance of 15·4 Å, which is roughly in keeping with experimental observation.

Our main focus, however, is in nano-scale phenomena involving the cooperative behaviour of multiple defects. A prime example, and one which illustrates the strengths of the method, is nanoindentation, where the penetration of the indenter is accommodated by the nucleation at the surface—and subsequent propagation into the crystal—of a small number of discrete dislocations. The multiple-scale character of this boundary value problem renders it awkward for analysis by either atomistic or continuum methods. By contrast, our combined atomistic/continuum approach permits the individual dislocations to be followed as they are nucleated under the indenter and driven into the crystal, while, simultaneously, yielding the response of the system at the nano-scale, e.g. in the form of the relationship between applied force and depth of indentation (Tadmor, Phillips and Ortiz 1996). In this class of applications lies the primary scope of the method.

Fig. 21

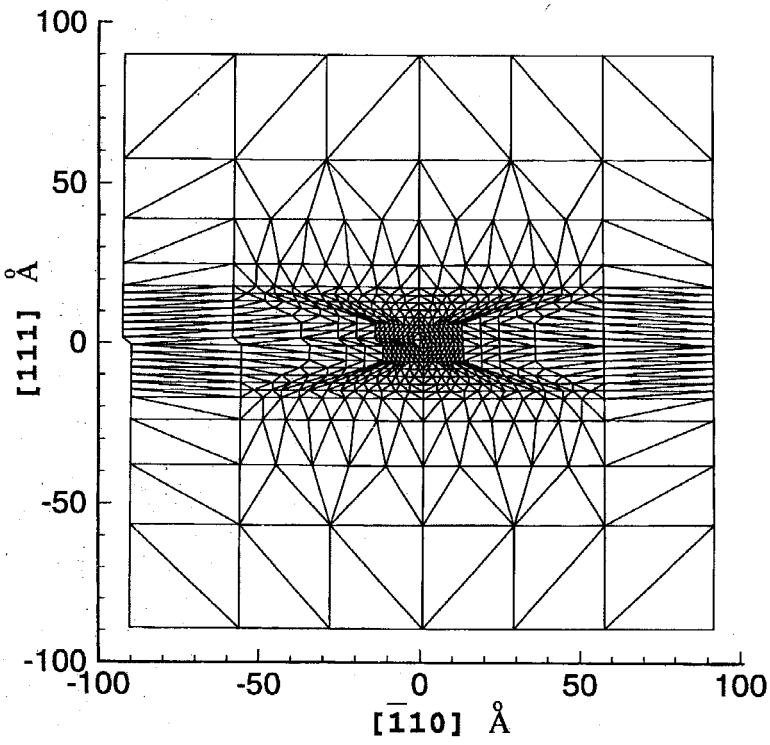

(*a*)

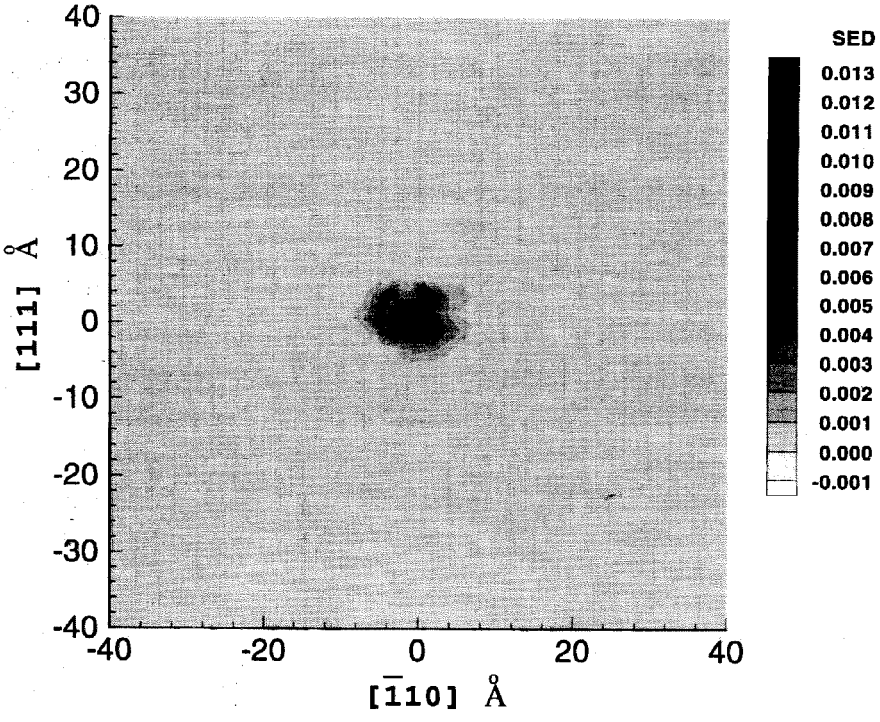

(*b*)

Primary edge dislocation QC model. (*a*) Initially distorted FEM mesh. (*b*) Close-up of edge dislocation core initial strain energy density (eV Å^{-2}).

Fig. 22

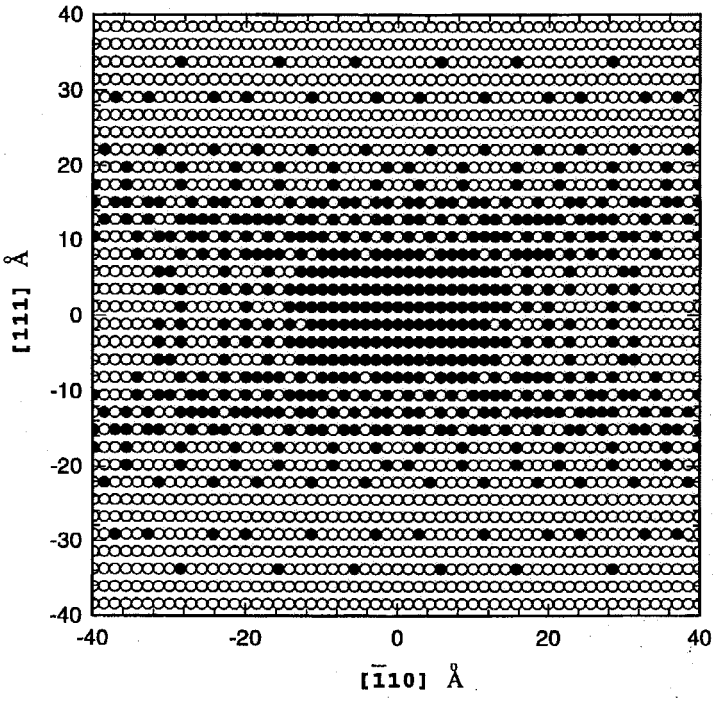

Representative atoms (black) superimposed on the atoms of the underlying crystal (white).

Fig. 23

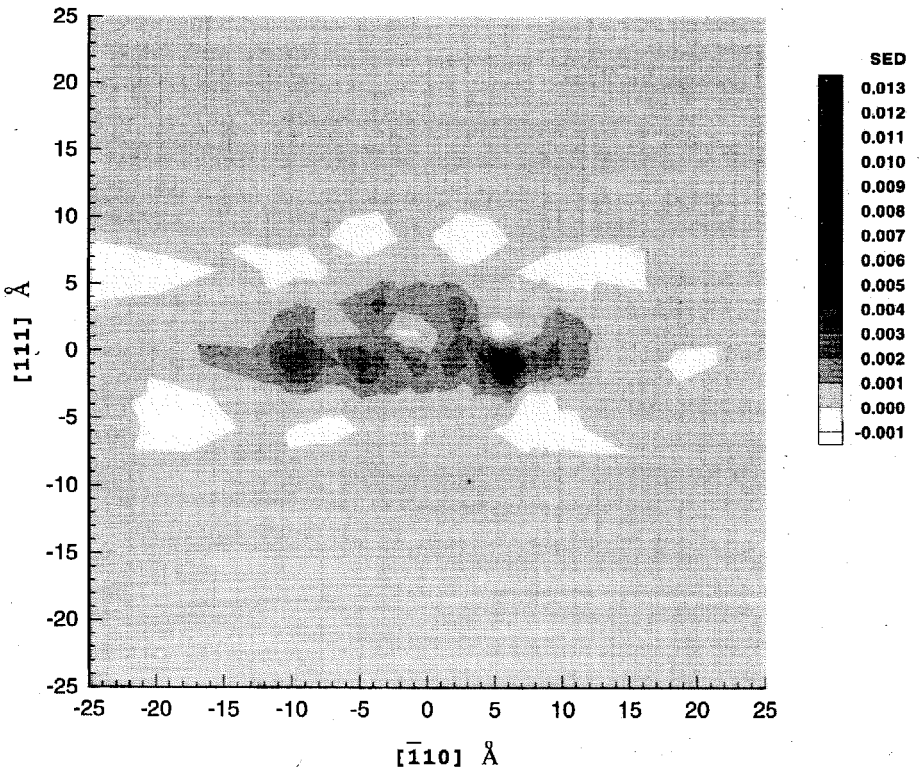

Relaxed primary edge discloation (QC solution), strain energy density (eV $Å^{-2}$) near core.

Fig. 24

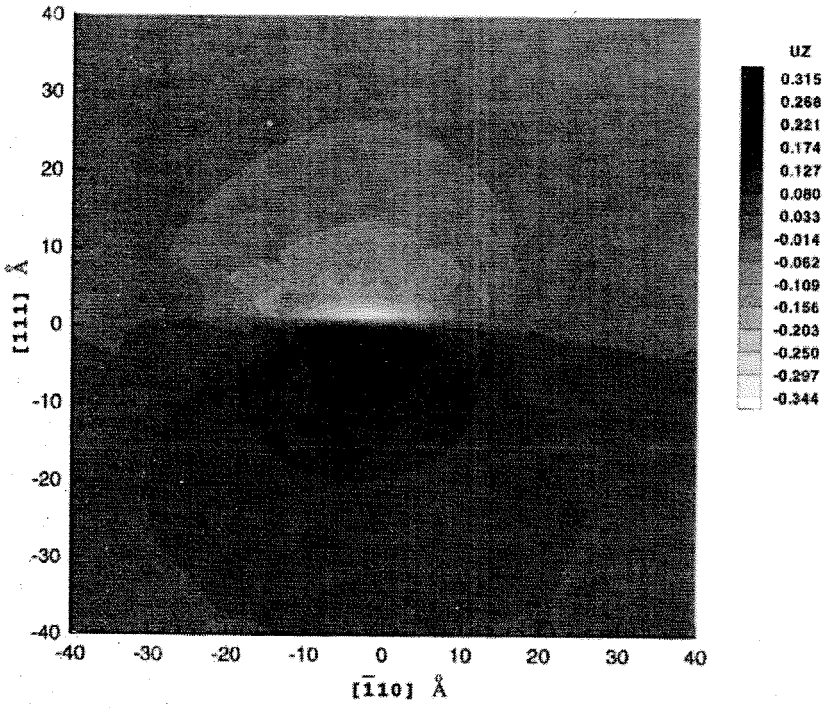

Out-of-plane displacement near core of relaxed primary edge dislocation (QC solution).

Fig. 25

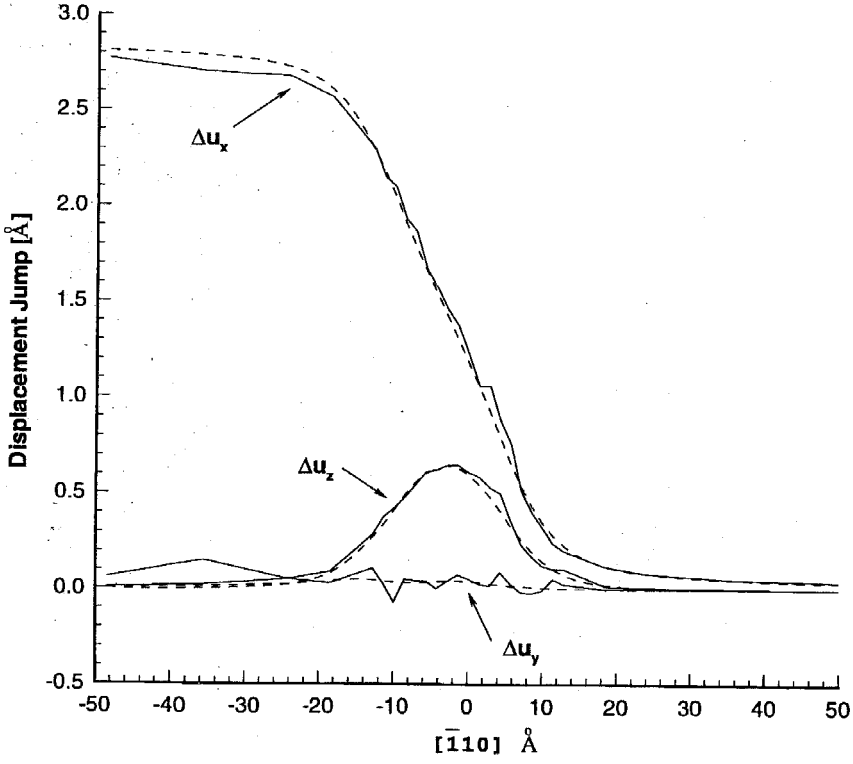

Comparison of LS (– – –) and QC (——) displacement jumps across the slip plane (Δu_x = slip, Δu_y = opening displacement, Δu_z = out-of-plane displacement), for relaxed primary edge dislocation core.

ACKNOWLEDGMENTS

The authors gratefully acknowledge support from the AFOSR through grant F49620-92-J-0129. R. P. gratefully acknowledges support from NSF under grant number CMS-9414648. This material is also based upon work supported by the National Science Foundation under the Materials Research Group grant no. DMR-9223683. We appreciate comments by R. Clifton, J. Weiner, R. Miller and V. Shenoy.

REFERENCES

ARIAS, T. A., and JOANNOPOULOS, J. D., 1994, *Phys. Rev. Lett.*, **73**, 680.
BALL, J. M., and JAMES, R. D., 1987, *Arch. Rat. Mechn. Anal.*, **100**, 15.
BASSANI, J. L., VITEK, V., and ALBER, I., 1992, *Acta metall. mater.*, **40**, S307.
BREDE, M., 1993, *Acta metall. mater.*, **41**, 211.
CHIAO, Y.-H., and CLARKE, D. R., 1989, *Acta metall.*, **37**, 203.
CHIPOT, M., and KINDERLEHRER, D., 1988, *Arch. Rat. Mech. Anal.*, **103**, 237.
CHRISTIAN, J. W., 1983, *Metall. Trans.*, **14A**, 1237.
CUITIÑO, A. M., and ORTIZ, M., 1992, *Modelling Simul. Mater. Sci. Engng*, **1**, 225.
DACOROGNA, B., 1989, *Direct Methods in the Calculus of Variations* (Berlin: Springer-Verlag).
DAW, M. S., and BASKES, M. I., 1983, *Phys. Rev. Lett.*, **50**, 1285.
ERCOLESSI, F., and ADAMS, J., 1993, *Europhys. Lett.*, **26**, 583.
ERICKSEN, J. L., 1984, *Phase Transformations and Material Instabilities in Solids*, edited by M. Gurtin (New York: Academic Press).
FONESCA, I., 1988, *J. Math. Pures Appl.*, **67**, 175.
GALLEGO, R., and ORTIZ, M., 1993, *Modelling Simul. Mater. Sci. Engng*, **1**, 417.
GURTIN, M. E., 1981, *An Introduction to Continuum Mechanics* (New York: Academic Press).
HARVEY, S., HUANG, H., VENKATARAMAN, S., and GERBERICH, W. W., 1993, *J. mater. Res.*, **8**, 1291.
HIRTH, J. P., and LOTHE, J., 1992, *Theory of Dislocations*, second edition (Malabar, FL: Krieger).
HUGHES, T. J. R., 1987, *The Finite Element of Method* (Englewood Cliffs, NJ: Prentice-Hall).
KOHLHOFF, S., GUMBSCH, P., and FISCHMEISTER, H. F., 1991, *Phil. Mag.*, **64A**, 851.
KUNIN, I. A., 1982, *Elastic Media with Microstructure* (Berlin: Springer-Verlag).
MARSDEN, J. E., and HUGHES, T. J. R., 1983, *Mathematical Foundations of Elasticity* (Englewood Cliffs, NJ: Prentice-Hall).
MILLS, M. J., DAW, M. S., and FOILES, S. M., 1994, *Ultramicroscopy*, **56**, 79.
MILSTEIN, F., 1982, In *Mechanics of Solids*, edited by H. G. Hopkins and M. J. Sewell (Oxford: Pergamon Press).
PHARR, G. M., OLIVER, W. C., and CLARKE, D. R., 1990, *J. Electron. Mater.*, **19**, 881.
PRESS, W. H., TEUKOLSKY, S. A., VETTERLING, W. T., and FLANNERY, B. P., 1992, *Numerical Recipes in FORTRAN*, second edition (Cambridge University Press).
RICE, J. R., 1992, *J. Mech. Phys. Solids*, **40**, 239.
SLOAN, S. W., 1987, *Adv. Engng Software*, **9**, 34.
SUTTON, A. P., and PETHICA, J. B., 1990, *J. Phys.: condens. Matter*, **2**, 5317.
TADMOR, E. B., PHILLIPS, R., and ORTIZ, M., 1996, *Langmuir* (in press).
WEINER, J. H., 1983, *Statistical Mechanics of Elasticity* (New York: Wiley).